

Anomalies and Fluctuations of Near-surface Air Temperature at Tianhuangping (Zhejiang), China, Produced by the Longest Total Solar Eclipse of the 21st Century Under Cloudy Skies

Marcos A. Peñaloza-Murillo ^{1,2}, Michael T. Roman ³, and Jay M. Pasachoff ^{2,4}, ¹ Universidad de los Andes, Facultad de Ciencias, Departamento de Física. Mérida 5101, Edo. Mérida, Venezuela; map4@williams.edu ² Williams College, Department of Astronomy. Williamstown, MA 01267, USA; eclipse@williams.edu ³ The University of Leicester, Department of Physics and Astronomy. Leicester LE1 7RH, UK; mr359@le.ac.uk ⁴ Carnegie Observatories, Pasadena, CA 91101, USA Received 2020 July 19; accepted 2020 August 26; published 2020 October 14

Abstract

During a total eclipse of the Sun, the solar disk blocked by the lunar disk produces an instant and strong decline of energy at the surface. This loss of energy leads to a decreasing air temperatures near the surface. Anyone under a completely clear sky, with a total solar eclipse (TSE) in progress, feels a cooling, whose minimum is reached a few minutes after totality. This drop in temperature is known as an anomaly and this delay is called thermal lag. During a TSE air temperature changes appreciably not only in magnitude but also in timing, depending on weather and geographical conditions. If the eclipse is partially or totally obscured by clouds, some effects are produced on the thermal lag. Under clear skies, the temperature response lags behind the change in solar flux as one expects in TSE; however, under cloudy skies, the lag can reverse in early and/or late stages of partial phases. The normal heating of the surface by the Sun, which drives turbulent motion in the air layer near the surface, is disrupted during the eclipse. The 2009 TSE in China provided an opportunity to have a look at these kinds of perturbations caused by this eclipse. In this paper, the second of a series of three, we analyze the near-surface air temperature response, at three different heights over the ground, recorded by the Williams College expedition under meteorological conditions characterized by cloudy skies during the longest total solar eclipse of the 21st century on 2009 July 22, at Tianhuangping (Zhejiang), China. An analysis of the relationship between solar radiation and air temperature was made by applying a study previously published in the first paper of this series in which we evaluated the cloudiness contribution in estimating the impact on global solar radiation throughout this phenomenon at that site. The analysis of this response includes linear and absolute negative anomalies as well as fluctuations, which was undertaken through a statistical study to get information on the convection activity produced by the latter. The fluctuations generated by turbulence were studied by analyzing variance and residuals. The results, indicating a steady decrease and recovery of both perturbations, were consistent with those published by other studies for this total solar eclipse.

Key words: Atmospheric effects - Clouds - Earth atmosphere - Solar-terrestrial interactions - Total eclipses Online material: color figures

1. Introduction

The observation and study of near-surface air temperature (NSAT) variation during a solar eclipse has always played a relevant direct or indirect role in atmospheric science since it first began to be measured in the nineteenth century (Brerenton 1834; Alexander 1854) (see also Table S1 in Supplementary on-line material of Peñaloza-Murillo & Pasachoff (2015) for some other historical references). Subtle atmospheric effects should be expected and detected due to the relatively rapid change in insolation and temperature, and others ambient variables, during a total solar eclipse (TSE) (for an extensive (but not exhaustive) list of references, see Tables S2–S3 in Supplementary On-line material of Peñaloza-Murillo & Pasachoff 2015). The greatest thermal

response and consequent effects would be expected during TSEs with greatest durations but under clear skies (Aplin & Harrison 2003); therefore, relatively long-duration TSEs should provide the best opportunity to measure and analyze atmospheric response under this condition. Scientific observations at total solar eclipses were summarized by Pasachoff (2009, 2017).

According to Meeus (2002) and Espenak (2014) between 2001 and 2100, there are eleven TSEs with maximum duration greater than five minutes, with none more than seven minutes (see Table 1 of Peñaloza-Murillo & Pasachoff 2018 for TSEs with maximum totality duration greater than five minutes during this century). The longest one, with up to 6'40" of totality, took place in 2009 July 22, with its longest duration somewhere in the western Pacific Ocean. Part of its

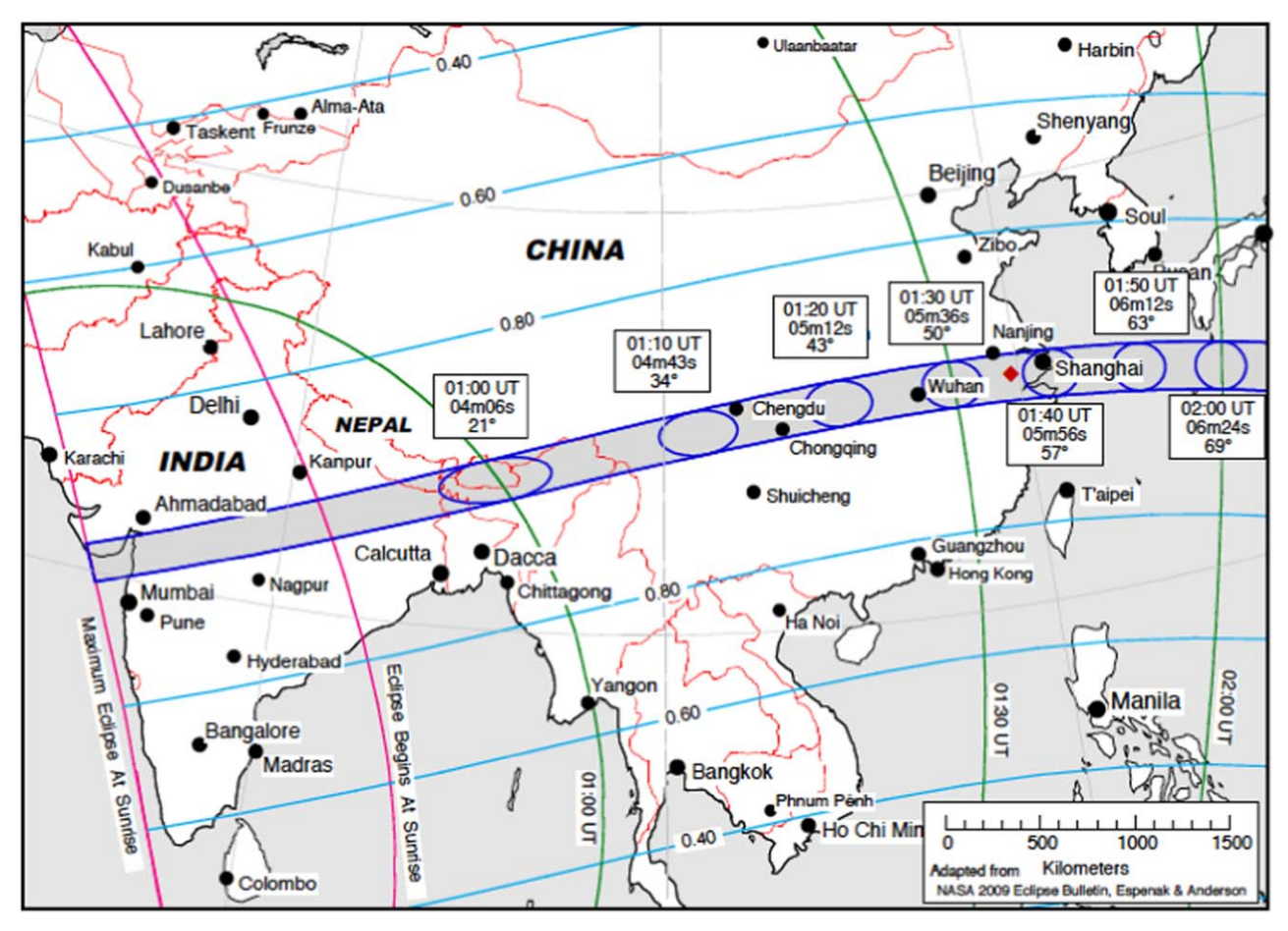


Figure 1. The umbral and penumbral region of the solar eclipse on 2009 July 22, over Asia. The totality path passed over India, Nepal, Bangladesh, Bhutan, Burma, China, and some Japanese islands (Espenak & Anderson 2008). Our observation site, in the mountains near Hangzhou west of Shanghai, had nearly the longest possible duration available on a large land mass (see Peñaloza-Murillo & Pasachoff 2018). The red diamond indicates approximately our observation site. (Adapted from Espenak & Anderson 2008. Image stated to be in the public domain.)

shadow path passed over India, Nepal, Bhutan, Bangladesh, China and some Japanese islands in the morning (Figure 1). The expedition of Williams College—Hopkins Observatory to observe this event went to China (Pasachoff et al. 2011), where its scientific equipment was set up at Tianhuangping reservoir (Anji, Zhejiang), to be close to as far east as possible on land before the path of totality went over the ocean (see http://web.williams.edu/astronomy/eclipse/eclipse2009/2009 total/index.html).

NSAT measurements were taken there at three different heights over the ground and, in this study, they are presented and analyzed following the goals and the general procedure described and used in a previous paper (Peñaloza-Murillo & Pasachoff 2015) in which an air-cooling analysis was made based on the air temperature observations taken during the first TSE of the 21st century on 2001 June 21, at Lusaka, Zambia (Africa) by the Williams College—Hopkins Observatory

expedition to Africa, and in another subsequent paper by Peñaloza-Murillo & Pasachoff (2018) in which cloudiness and solar radiation were also analyzed during this TSE of 2009, the longest one of the 21st century, in China.

2. The Longest TSE of the 21st Century at Tianhuangping (Zhejiang), China: Local Circumstances

2.1. Local Geographical Data and Astronomical Circumstances

The site selected for the observations were the grounds of the Tianhuangping pumped-storage power station located in Anji County, Zhejiang Province, near Hangzhou, about 175 km to the west of Shanghai. This station has an upper reservoir or artificial lake on the top of a mountain, surrounded by green bamboo forests. The geographical coordinates of the site are

Table 1
Astronomical and Geographical Circumstances for the TSE of 2009 July 22, at Tianhuangping (Mt. Anji), Zhejiang, China

Circumstances	Value
Longitude	119°35′28″E
Latitude	30°28′07″N
Altitude	809 m
Sunrise	05:12:53
1st contact	08:20:49.1 (8.35 am)
Sun altitude	38°.2
2nd contact	09:33:02.8 (9.55 am)
Sun altitude	53.°7
Mid-totality	09:35:53.3 (9.60 am)
Sun altitude	54°.3
Minimum apparent distance between	
lunar center and solar center (at totality)	$6.963 \times 10^{-5} \text{ rad}$
Occultation	100%
3rd contact	09:38:44.9 (9.65 am)
Sun altitude	55°.0
4th contact	10:57:59.5 (10.97 am)
Sun altitude	71°.2
Duration of totality	$5'42''2 \ (\sim 5.70 \ \text{minutes})$
Total duration of eclipse	2.62 hr (\sim 157.2 minutes)
Magnitude at mid-totality ^a	1.03071
Solar disk (semi-diameter)	$15'44''50 (4.7507 \times 10^{-3} \text{ rad})$
Lunar disk (semi-diameter)	$16'19.''9 (4.990 \times 10^{-3} \text{ rad})$
Moon/Sun size ratio	1.10328
Umbral depth	80.4%
Location into the shadow	\sim 30.88 km from the central line ^b
Shadow path width	$\sim \! 266.66 \; \mathrm{km^{b}}$
"minor axis"	\sim 262.5 km ^b
"major"	\sim 300.0 km ^b
Umbral velocity	0.872 km s^{-1c}
Sunset	19:02:17

Notes. The contacts and other instants are given in local time (LT = UTC + 8 hr).

119°35′28″ E, 30°28′07″ N and 890 m above sea level. Table 1 gives the astronomical and geographical circumstances for this event. From these data it can be observed that we are dealing with a TSE that occurred during the morning, which has significant implications for our analysis as will be shown later. The sunrise was at 05:12:53, first contact at 08:20:49.1, and 4th contact at 10:57:59.5. Contacts and other interval times are given in local time (LT = UTC+8 hr). The total phase occurred between 09:33:02.8 and 09:38:44.9. The duration of totality was \sim 5.70 minutes and the total duration of the whole eclipse was of \sim 2.62 hr. The site was about 30.88 km away from the central line with a width of totality of \sim 267 km and Xavier Juvier calculated a value of 0.872 km s⁻¹ for the umbra velocity at this particular place.

(http://xjubier.free.fr/en/site_pages/solar_eclipses/TSE_2009_GoogleMapFull.html?Lat=30.46861&Lng=119.59111&Elv=890.0&Zoom=5&LC=1).

When the center of the umbra reached the Indian-China border (at 01:05 UTC), the shadow's velocity was $1.8~{\rm km~s}^{-1}$; at Hubei province's capital Wuhan, just 20 km south of central line, the umbra's velocity was $1.0~{\rm km~s}^{-1}$ (at 01:27 UTC) (Espenak & Anderson 2008). The instant of greatest eclipse occurred at 02:35:19 UTC at 24°13′N and 144°07′E when axis of the Moon's shadow passed closest to the center of Earth.

2.2. Meteorological Circumstances

At that date, in the morning and during the event, the sky was mostly cloudy over the region of Zhejiang. Morning storms were followed by widespread cirrostratus and variable stratocumulus during the eclipse, followed by afternoon rain showers. Because of its importance in assessing the incident solar radiation on the ground and, therefore in the overall eclipse, this cloudiness, recorded with a wide-field camera, is quantified and analyzed in Peñaloza-Murillo & Pasachoff (2018). Table 2 gives some meteorological circumstances (and also photometric) corresponding to which this event took place, conveying information on variation of different variables throughout and surrounding the eclipse period. Note that NSAT measurements are given for three different heights above the ground: very close to the ground at 2 cm, close to the ground at 10 cm, and above the ground at 2 m. The photometric and relative-humidity information was taken from the measurements made by Stoeva et al. (2009) at the same observation site. These authors gave illumination values for three different directions in the sky (zenith, horizon and solar area).

Total reductions of 6.01 °C, 5.90 °C, and 4.37 °C in air temperature were observed at 2 cm, 10 cm, and 2 m, respectively, in duration intervals of \sim 80 minutes (1.30 hr), \sim 79 minutes (1.32 hr) and \sim 79 minutes (1.32 hr), respectively, between first contact and the instant of minimum temperature (see Table 2). This same feature was observed for the respective time lag: 7.98 minutes for the lower height and 7.08 minutes for the rest, measured from the beginning of totality (at second contact) when the direct solar radiation is first completely blocked by the Moon. Recall that thermal response of the air is not in phase with the solar radiation response. The drop in temperature during these lags were, respectively, 0.73 °C, 0.44 °C and 0.34 °C. Other reductions such as the maximum "linear anomaly" ΔT_{linear} , were 8.42 °C, 7.07 °C, and 5.27 °C, respectively (see Table 2). By applying a linear regression fit, this anomaly is related to a hypothetical temperature time series over the eclipse period, using observed temperatures at the time of first and last contacts (Segal et al. 1996 (see their Figure 3); Figure 2(b)). This linear time series is assumed to be representative of temperature observations in the absence of an eclipse. Thus, the linear anomaly is obtained by subtracting the value of the interpolated

^a The magnitude of a TSE is the amount of the solar disk's diameter covered by the lunar disk.

^b Espenak & Anderson (2008).

^c Value calculated by Xavier Juvier (see text).

Table 2
Meteorological and Photometric Circumstances of the Sky During the TSE of 2009 July 22, at Tianhuangping (Zhejiang), China

Meteorological Value				Instant/Time Interval/Duration	
Sky					
Cloudiness		Cloudy and variab	06:31–11:50 ^a		
Solar Radiation (W m ⁻²)					
At 1st contact, S_{1c}		\sim 620 b		08:20:49.1 (8.35 am)	
At 4th contact, S_{4c}		$\sim 760^{b}$		10:57:59.5 (10.97 am)	
Air Temperature(°C)					
At height	+2 cm	+10 cm	+2 m		
Around sunrise, T_1	22.56	22.82	$23.93 \ (\pm 0.30)$	05:12:06	
Maximum, $T_{\rm MAX}$	36.66	33.78	31.81	11:05:01/10:49:02/11:40:01	
At 1st contact, T_{1c}	30.57	30.82	29.34	08:21:06 (8.35 hr)	
Maxim. (before totality), T_{max}	31.36	31.69	30.14	08:27/08:26/08:26	
At 2nd contact, T_{2c}	25.28	23.35	25.31	09:33:05 (9.55 hr)	
"Mid-totality," $T_{\rm Mid}$	24.89	25.09	25.14	09:36:00 (9.60 hr)	
"3rd contact," T _{3c}	24.65	24.97	25.02	09:39:02 (9.65 hr)	
Minimum (after totality), T_{\min}	24.56	24.92	24.97	09:41:01/09:40:05/09:40:05	
At 4th contact, T_{4c}	35.31 33.16 31.13			10:58:01 (10.97 hr)	
At last measurement, T_f	28.27	27.04	25.23	14:54:02 (14.90 hr)	
$\Delta T' = T_{1c} - T_{2c}$ (reduction)	5.29			\sim 71.'98 (\sim 1.2 hr)	
$\Delta T'' = T_{2c} - T_{\min} (")$	0.73	0.44	0.34	$(\sim 7.98/\sim 7.08/\sim 7.08)^{c}$	
$\Delta T = \Delta T' + \Delta T''$ (reduction)	6.01	5.90	4.37	$\sim 80' (1.3 \text{ hr})/\sim 79' (1.32 \text{ hr})/\sim 79' (1.32 \text{ hr})$	
$T_{i,n-e}$ (interpolated, non-eclipse)	32.98	31.99	30.24	09:41:01/09:40:05/09:40:05	
$\Delta T_{\mathrm{linear}} = T_{h,n-e}$ - T_{min}	8.42	7.07	5.27	09:41:01/09:40:05/09:40:05	
$\Delta T_{\rm absolute} = T_{\rm max} - T_{\rm min}$	6.80	6.77	5.17	80'.01/74'.28/74'.28	
Relative Humidity (%)				, ,	
At first measurement, RH ₁		70		08:00:00	
Minimum, RH _{min}		60		08:43:00-09:10:00	
Maximum, RH _{max}		72		09:45:00	
At last measurement, RH _f		59		10:27:00	
$\Delta RH' = RH_1 - RH_{min}$		10		43′	
$\Delta RH' = RH_{max} - RH_{min}$	12			35′	
Wind speed				•••	
Photometric		Value		Instant	
Ilumination (lx)	Zenith	Horizon	Solar Area		
At first measurement, l_1	274	48	205	07:08:36	
Minimum, l_{\min}	17	4	120	09:34:50	
At last measurement, l_f	3095	518	3287	11:27:18	

Notes. Time is given as local (LT = UTC + 8 hr); China has one time zone. Air temperature measurements were taken at three different heights above the ground: 2 cm, 10 cm, and 2 m. Values of relative humidity and illumination (in three different directions) were taken from Stoeva et al. (2009). (For similar and different measurements made during this eclipse at Tianhuangping, and in other sites of China as well as in South Korea and India, see Pintér et al. 2010, He et al. 2010, Chen et al. 2011, Zainuddin et al. 2013, Kwak et al. 2011, Chung et al. 2010, Wu et al. 2011, Lu et al. 2011, Kumar 2014, Rao et al. 2013, Jeon 2011, Wang & Liu 2010 and Jeon & Oh 2011.)

temperature corresponding to that under no-eclipse condition $(T_{i,n-e})$ at the same time of that corresponding to the observed minimum temperature during the eclipse. The other anomaly, the "absolute anomaly" $\Delta T_{\rm absolute}$, were 6.80 °C, 6.77 °C and 5.17 °C, respectively (see Table 2), which involves calculating the difference between a pre-eclipse maximum temperature (between first and second contacts) and an eclipse period minimum temperature (see Figure 2(a)).

Changes in surface temperatures moves the air's water vapor content closer to saturation, increasing its relative humidity (RH). This time RH increased by 12% between 09:10:00 and 09:45:00 (Stoeva et al. 2009), corresponding from roughly 23 minutes prior to 6 minutes following totality. The ambient illumination was drastically reduced in all three directions by up to 17 lx, for the zenith; 4 lx for the horizon; and 120 lx, for the solar area (Stoeva et al. 2009). No wind data were available.

^a See Peñaloza-Murillo & Pasachoff (2018).

^b Values derived from calculations (see Figure 4 and also Figures 14 and 15 of Peñaloza-Murillo & Pasachoff 2018).

^c These are the lags for air temperature reduction $\Delta T''$ at specified heights measured from the time of second contact. For the same spot, but in a different environment where their measurements were taken, Stoeva et al. (2009) observed a lag if 1 minutes after the end of total phase, say, a lag of 6.70 minutes from second contact (when the solar radiation is switched off), supposedly, for three different heights above the ground, namely, of +10 cm, +50 cm and +2 m.

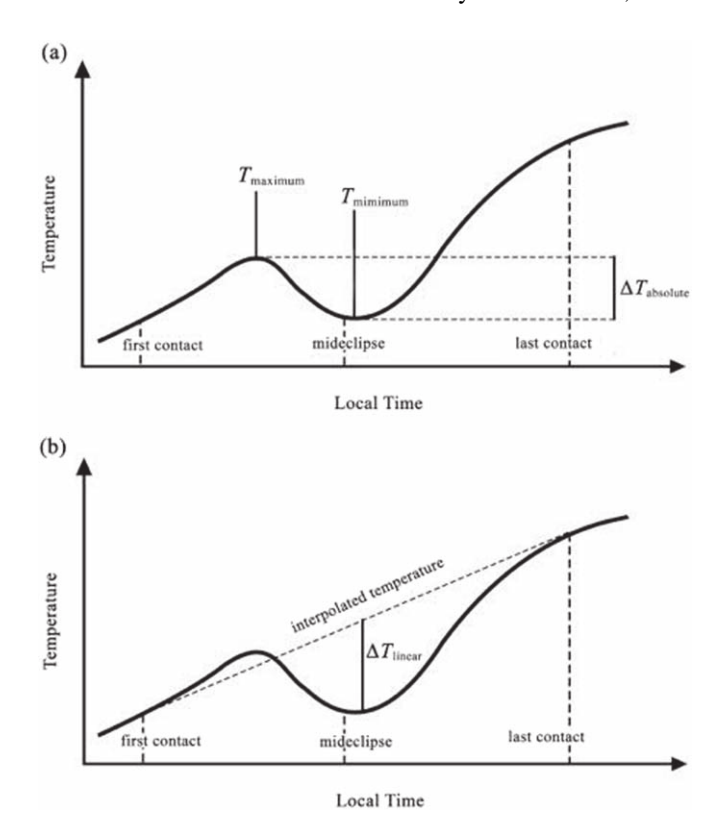


Figure 2. The graphs shown in this figure illustrate schematically how absolute (a) and linear (b) anomalies are defined. Note that $\Delta T_{\rm linear} > \Delta T_{\rm absolute}$. (Reprinted with permission from Clark 2016.)

3. Instrumentation and Air Temperature Measurements

Ambient air temperature was measured with a MicroDAQ HOBO U12 data logger with 4 external inputs suitable for multiple parameters of outdoor environmental measurements and recording. It is capable of measuring and storing up to 43,000 12 bit samples/readings with an operating range of -20 °C-70 °C and with a resolution of 0.6 mV. It has an adjustable sampling rate of 1 s to 18 hr. More details about this equipment can be found in https://www.microdaq.com/ manufacturers/onset-computer/hobo-data-loggers/u12-series. php. A calibration checking of the instrument was carried out days prior to the event. The temperature sensors were installed at three different heights above the ground (see Table 2), surrounded by green vegetation, and shielded from direct sunlight using small shades and a natural extra-shielding by clouds because the sky was mostly cloudy that morning (see Peñaloza-Murillo & Pasachoff (2018) and https://www. youtube.com/watch?v=XLdb1b72GVM).

In particular, the location was a mostly shady but well ventilated bamboo grove, carefully chosen, with long grass and leafy green vegetation interspersed. In addition to the shade provided by nearby trees, the sensors were shielded from direct

solar radiation by loosely encompassing radiation shields constructed of an opaque thick paper. Uncertainties in the measurements due to our local environmental location and shielding material are difficult to quantify, but Krause & Dodrill (1986) suggest noise introduced through improper shielding is typically on order of a few tenths of a degree. We considered an error of this magnitude to be reasonable for our measurements.

Figure 3 presents a general view of temperature variation from 06:13:00 to 14:44:00. Readings were recorded every 63 s. An inspection of this figure shows the effect of the eclipse on this variable in the morning after the eclipse ended as well as the effect of bad weather after midday and during the first part of the afternoon. In Figure 4, we show only the section corresponding to NSAT variation during the eclipse from first to fourth contact, roughly from 08:21 to 10:58 at 1 minute intervals. Graphically, all three curves show a delay or lag in relation to the central phase, which has been quantified from the data (see also Table 2). The drop of temperature is more significant at 2 cm height than the other two heights. Generally, the surface layer is the warmest due its contact (and consequent thermal conduction) with the radiatively heated ground; therefore, it cools down more rapidly (see Figure 3).

The whole pattern displayed by our measurements in Figure 3 is typical for cloudy or/and rainy weather. It is quite similar (mainly after 11:00 up to past 14:00) to that published by Pintér et al. (2010) for the same TSE and to that published by Winkler et al. (2001) for the 1999 TSE at Garching, Germany.

4. Analysis of the Relationship Between Solar Radiation and Air Temperature

In a previous paper, Peñaloza-Murillo & Pasachoff (2015) presented detailed methodological considerations in relation to the problem of how to analyze the relationship between solar radiation and air temperature during a total solar eclipse following the works of Phillips (1969), Szałowski (2002), Tzanis (2005), and Pintér et al. (2008), though those previous works were for relatively clear skies. The reader is referred to all these papers for details. Yet this time we face an additional problem: how to analyze mathematically this relationship under significant cloudy skies as those we had at Tianhuangping (Peñaloza-Murillo & Pasachoff 2018).

The umbra of the last TSE of the 20th century, which took place on 1999 August 11, pass over Western, Central, and Eastern Europe, under variable cloudy conditions. A considerable number of papers, however, were published on the meteorological effects of this eclipse (see Table S1, on-line supplementary material of Peñaloza-Murillo & Pasachoff 2015) but none of them attempted to undertake a specific mathematically analysis between solar radiation and local NSAT. The worst region for observing this eclipse was England, where the sky was heavily cloudy or practically overcast (e.g., Camborne, Cornwall); even so, some micrometeorological measurements

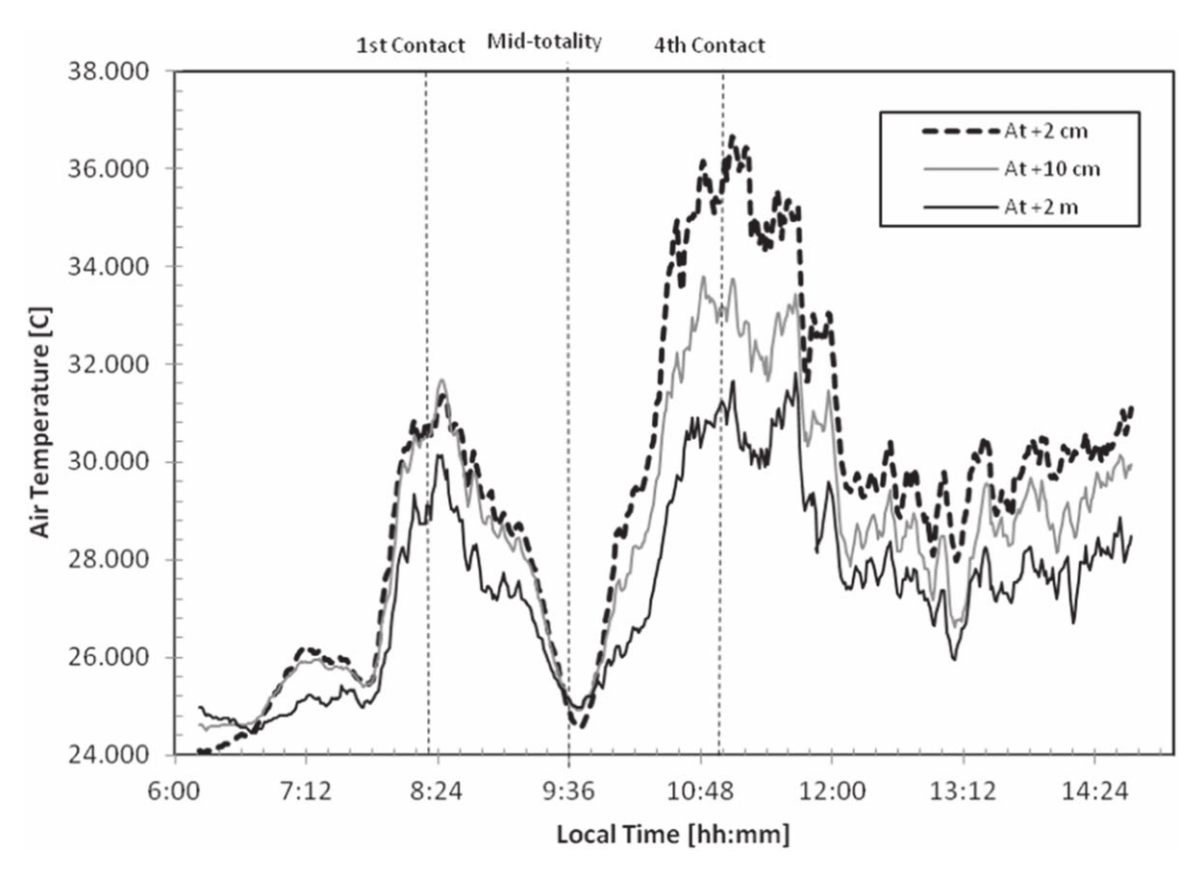


Figure 3. Air temperature variation ($^{\circ}$ C), at three different heights, during the day of TSE in 2009 July 22, in Tianhuangping (Mt. Anji, Zhejiang), China. The measurements were stopped at around 14:40 due to bad weather (overcast and rain). The effect of the occultation on measurements is clearly seen as well as the effect of bad weather around 11:30 onwards. These noisy patterns are the result of different combined factors like cloudiness, convection, altitude, solar radiation, etc., that intervene in determining the temperature variation over time. Uncertainties are estimated to be ± 0.30 $^{\circ}$ C.

were made at several sites in that country (e.g., Hanna 2000; Leeds-Harrison et al. 2000; Morecroft et al. 2000; Aplin & Harrison 2003). In particular the latter authors tried to interpret theoretically their temperature measurements in the light of the diurnal-cyclones theory and the cold-core eclipse-cyclone hypothesis proposed by Clayton (1901) at the onset of the previous century.⁵

Our first challenge was to obtain a theoretical model of solar radiation under cloudy and eclipse conditions for our observation site from which we can derive theoretical models for NSAT measurements presented in the curves of Figure 4. For these goals it was necessary first to get the occultation and obscuration function, via limb-darkening integration as was done by Peñaloza-Murillo & Pasachoff (2018) and to which the reader is referred for details. Our challenge now is to apply the pioneering Phillips's method (Phillips 1969), in combination with that of Peñaloza-Murillo & Pasachoff (2018), to retrieve the temperature profile directly from a radiative model of the

solar radiation's collapse and recovery during the eclipse process, this time total, but under cloudy conditions.

Phillips's method is described more thoroughly in Peñaloza-Murillo & Pasachoff (2015). It is based on a sort of calibration curve of the type "air temperature versus solar radiation" from which we can extract the air temperature during the phenomenon. In this case, clouds of different types and heights affected the solar radiation before, during, and after the eclipse (Peñaloza-Murillo & Pasachoff 2018). Therefore, our first task, of this part of the investigation, was to formulate a solar-radiation model under cloudy conditions, as if the eclipse had not happened, in order to be taken subsequently as such in the eclipse situation, as was obtained by Peñaloza-Murillo & Pasachoff (2018) (see Figure 5).

4.1. NSAT Profiles

To a first approximation the daily ambient air temperature, and in particular the NSAT, for a given location, is directly related to daily global radiation, modulated, of course, by many factors including weather and geography. The idea that this

⁵ To update research on Clayton's cold-core cyclone hypothesis, see Gray & Harrison (2012).

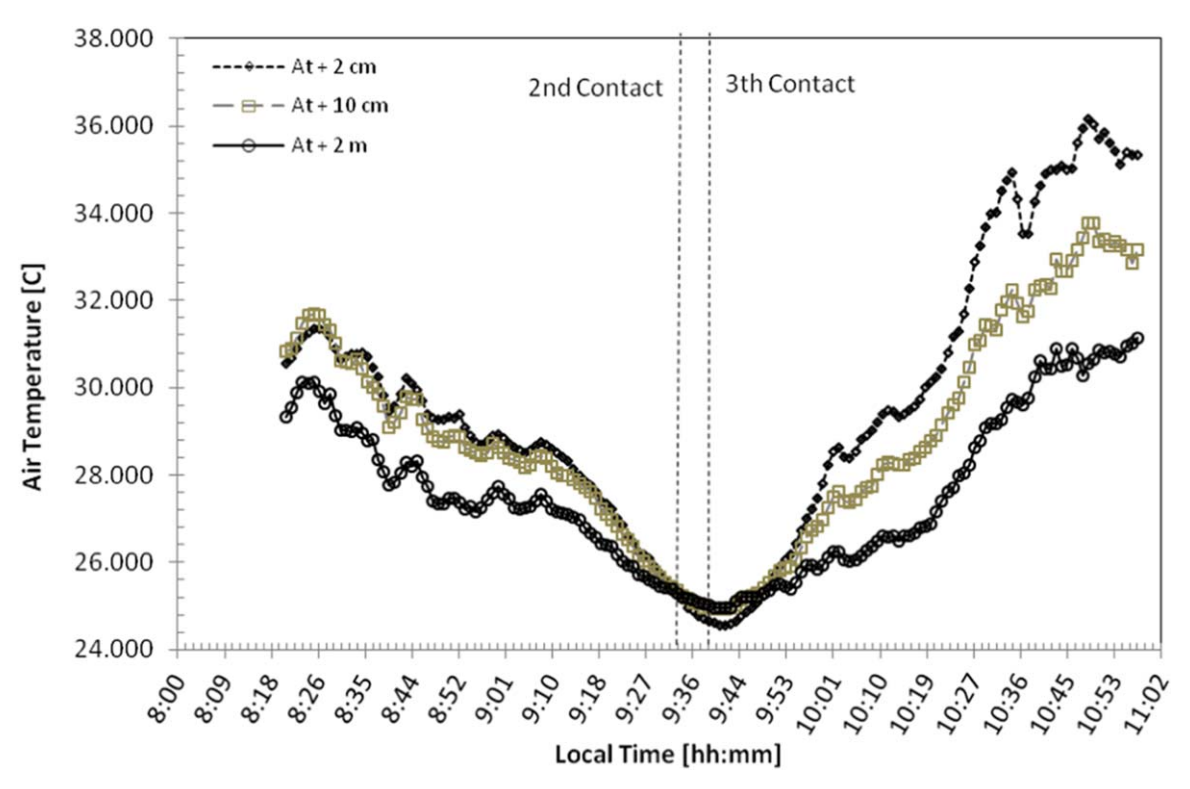


Figure 4. Air temperature variation (°C) during the TSE of 2009 July 22, at Tianhuangping at different indicated heights. First contact was at 08:20:49.1 and fourth one at 10:57:59.5. Totality occurred between 09:33:02.8 (2nd contact) and 09:38:44.9 (3th contact).

relation could be used to model air temperature during a solar eclipse under clear skies came first from the work of Phillips (1969). It has successfully been applied by Peñaloza-Murillo & Pasachoff (2015) in a cloudless situation. Phillips proposed a methodology based on the construction of a plot relating air temperature to global solar radiation, omitting temperatures measured during the eclipse. Global solar radiation values were obtained from the corresponding model. In this way, a sort of calibration curve of the type "Air Temperature versus Global Solar Radiation" was produced by interpolating a final regression straight line in the sector of the plot corresponding to the omissions of eclipse-related values of air temperature. Given the values of this radiation provided by the model during the eclipse (Figure 5), one can retrieve air temperature values by reading out the calibration curve.

For every temperature profile of Figure 4 we constructed calibration charts, which provided the calibration curves (Figure 6). From these curves, the instantaneous thermal response of the air, at the three specified heights, were found as depicted in Figure 7. Here, instantaneous thermal response stands for the air temperature that should be attained in absence of any kind of delay or lag, in phase with the solar radiation change and also with the obscuration function. Defined in this way, this variable can be called "instantaneous temperature," $T_{\rm inst}$.

In comparing these instantaneous profiles to measurements as shown in Figures 8–10, (see also Figures 11(a), 12(a) and 13(a)), some interesting features emerge. The measurements exhibit appreciable fluctuations or instabilities between 08:21 and 09:07 for +2 cm and, from 08:21 to 09:10 for both +10 cm and +2 m. The fluctuations begin to disappear as totality approaches (09:37) with little to no fluctuations from 09:08 to 10:07 at +2 cm, from 09:11 to 10:03 at +10 cm and between 09:11 and 09:48 at +2 m. The fluctuations appear again from these points until 10:57, around fourth contact. The fluctuations are stronger during the first phase of the eclipse than in the final phase. These fluctuations are interpreted as convective activity in the surface layer (to be analyzed in the next section). The reduction in convective instability is likely a direct result of the eclipse. Surprisingly, during the period of convective turbulence and consequent temperature fluctuations preceding totality (i.e., prior to \sim 9:16 LT), the measured temperatures appeared cooler than expected from our instantaneous radiative model; this suggests that the atmospheric cooling was enhanced by dynamical processes not captured in our radiative model (e.g., local advection, vertical mixing) or simply that our radiative model failed to completely account for the observed cloud cover during this period. This effectively results in cooling that appears to precede that seen in our instantaneous model, and clearly illustrates how clouds can alter the observed temperatures. In a

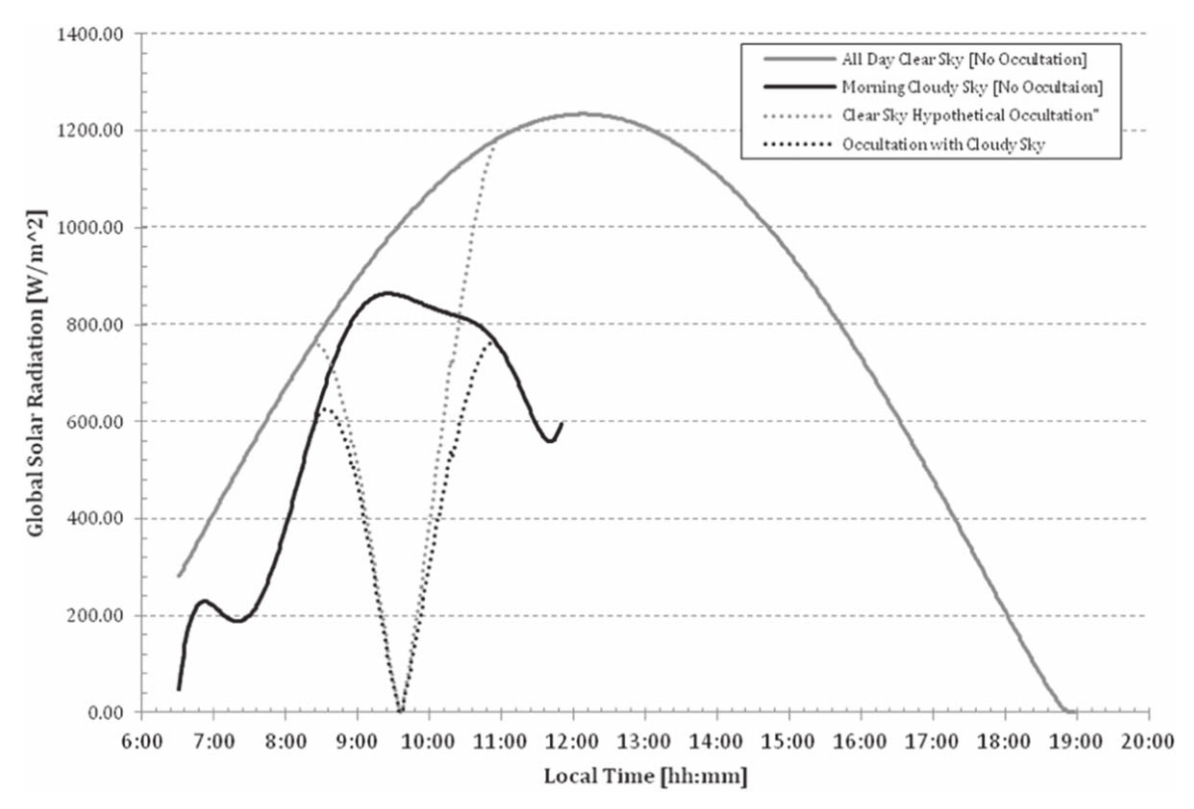


Figure 5. Theoretical model for global solar radiation (W m⁻²) where the eclipse is considered under cloudless (gray lines) and cloudy (black lines) conditions at Tianhuangping during the morning in 2009 July 22, obtained by Peñaloza-Murillo & Pasachoff (2018). (Reprinted with permission from Peñaloza-Murillo & Pasachoff 2018. © AGU 2018.)

cloudless sky, however, this effect does not occur, as has been shown in our previous investigation of the African TSE of 2001 (Peñaloza-Murillo & Pasachoff 2015) and others.

In above context, it is worthy to note that Aplin & Harrison (2003) found a similar effect at Camborne (England), during the TSE of 1999 August 11, under overcast skies. The temperature minimum at that eclipse actually occurred before totality was reached and not after, as expected. This inverse delay can be referred to as a "negative lag" due to cloudiness. In the present case some negative lags are observed clearly in Figures 8, 10 and to a lesser extent in Figure 9. As long as the effect of decreasing cloudiness tended to be small (as it was observed around totality), the measurements, in a first stage and up to some point, came earlier than the theoretical values (negative lag); afterwards and inversely, the theoretical values came first, that is to say earlier, then the increasing values of the temperature measurements, as it is normally expected (positive lag). Toward the final partial phase after totality, at +2 cm(Figure 8), we can observe another lag inversion. This temporal inter-changeability between negative and positive lag is the result of the combined effect of clouds on solar radiation

variability, during the eclipse, and the natural thermal complex response of the ambient air to the phenomenon (Rabin & Doviak 1989). See Figures 8–10 for more details.

For the remainder of this work, we will focus on analyzing the NSAT fluctuations. The analysis and quantification of negative lag found at the different heights in this research will be made in future work.

5. Analysis of Air Temperature Fluctuations

The notable existence of NSAT fluctuations, of different magnitude, during the eclipse is evident for the three sensing situations presented in Figure 4 (see also Figures 8–10). These fluctuations are a recognizable phenomenon attributable to convective turbulence, which in general tends to disappear or minimize as long as the sunlight diminishes (Nieuwstadt & Brost 1986) including that due to the eclipse (Kadygrov et al. 2013), and return to normal conditions following the eclipse when this event occurs in the morning. This same recovery would likely not be seen in an afternoon eclipse (Peñaloza-Murillo & Pasachoff 2015). This convection suppression led to a more stable condition of the air in a certain period of time around totality, for the three cases considered here. The mechanism behind these changes is a product of the abrupt

 $^{^{6}}$ This aspect is possibly a result of the eclipse itself, perhaps because of the cloudiness.

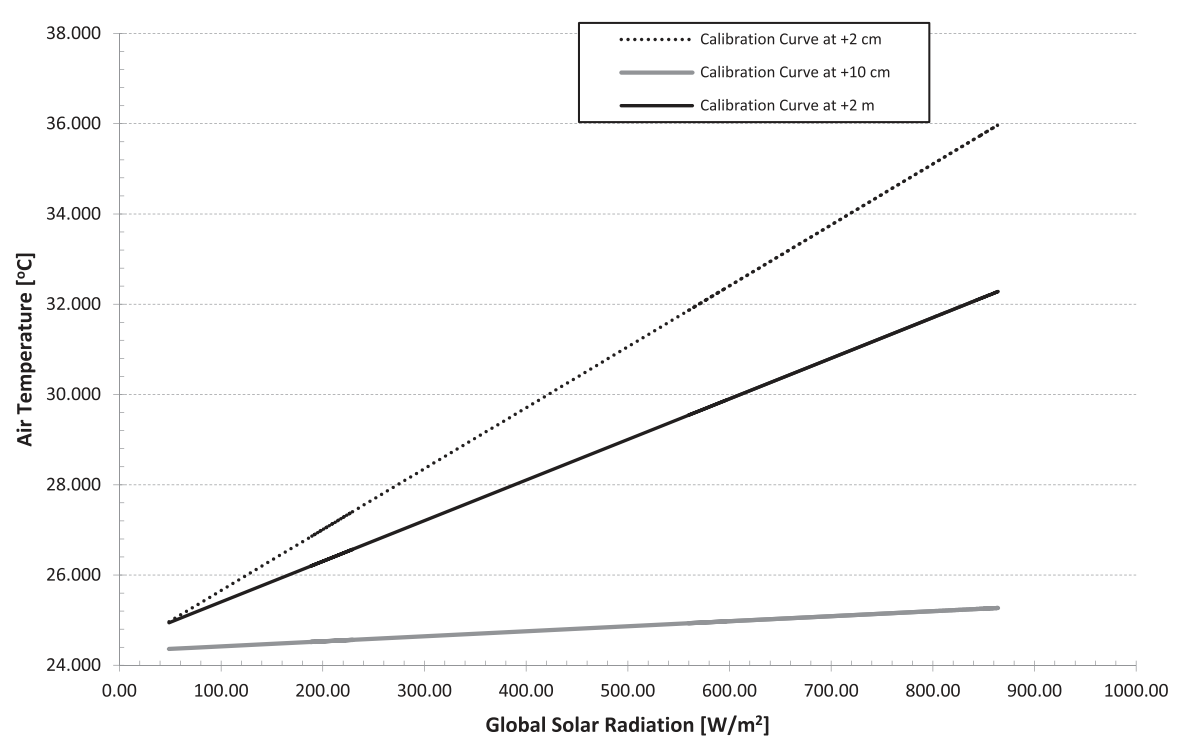


Figure 6. Approximate calibration curves for the three indicated heights above the ground. These curves enable converting solar flux during the eclipse (Figure 4) into the so-called instantaneous temperature (Figure 7). They were estimated following the procedure of Phillips (1969), which was subsequently applied by Peñaloza-Murillo & Pasachoff (2015).

alteration in insolation, causing cooling in the surface layers of the atmosphere and damping of atmospheric turbulence from the surface upwards. Mixed with these fluctuations, there are those coming from cloudiness variation.

To analyze these fluctuations, as in our previous work (Peñaloza-Murillo & Pasachoff 2015), we follow the method of Szałowski (2002) based on a variance analysis and residuals calculations of the convective turbulence. In doing so, it is convenient to make our analysis separately to each of the three cases involved in this investigation: case I, at 2 cm; case II, at 10 cm; and case III, at 2 m above the ground, respectively.

5.1. Case
$$I(+2cm)$$

Focusing on the measurements of Figure 4 in detail (or Figure 8), we observe in this case two temporal segments in which the convective activity is remarkable. The first, at the beginning, goes from 08:21 to 09:06. The other at the end, goes from 10:02 to 10:57. In between, we have the stable segment corresponding to the interval 09:07–10:02. We note, however, that the first exhibits appreciable fluctuations in the sub-interval 08:21–08:46 (sub-interval A_I) and smaller ones in the next sub-interval 08:47 to 09:06 (sub-interval B_I). For the last segment, we have similar behavior. In the sub-interval 10:03–10:35 (sub-interval D_I), we have small fluctuations, and in the final sub-interval, from 10:36 to 10:57 (sub-interval E_I), the convective activity becomes increasingly higher again in accordance to

what one can expect late in the morning. The middle stable segment is designed, then, as sub-interval $C_{\rm I}$. Under this temporal distribution of five sub-intervals, to some extent arbitrarily chosen on the base of an only visually different temperature fluctuation, we proceed to apply the method of Szałowski (2002) to each of these sub-intervals.

The method states that the variance is a common and good parameter to measure directly temperature fluctuations owing to convectional turbulent activity but certain conditions apply. Szałowski (2002) defines the temperature fluctuation as:

$$T'(t) = T(t) - \overline{T}(t), \tag{1}$$

where $\overline{T}(t)$ represents the mean temperature and T(t) represents the measured temperature at time t. If this mean varies negligibly, as happens especially for short measurements series investigating high frequency temperature fluctuations in stable weather conditions, the analysis of variance $\sigma_{T'}$ is direct. If, on the other hand, the fluctuation process is random, it implies that the mean of fluctuations is zero, $\overline{T}'=0$, allows for estimating $\overline{T}(t)$ by least-squares fit. Then, $\overline{T}(t_i)=T_{\text{pred}}$ and the residuals, for each realization of temperature measurement in time instant t_i , are given by,

$$T'(t_i) = T_{\text{obs}}(t_i) - T_{\text{pred}}(t_i), \tag{2}$$

where T_{pred} is the regression equation obtained via that fit. Here $T_{\text{obs}}(t_i)$ is the measured temperature.

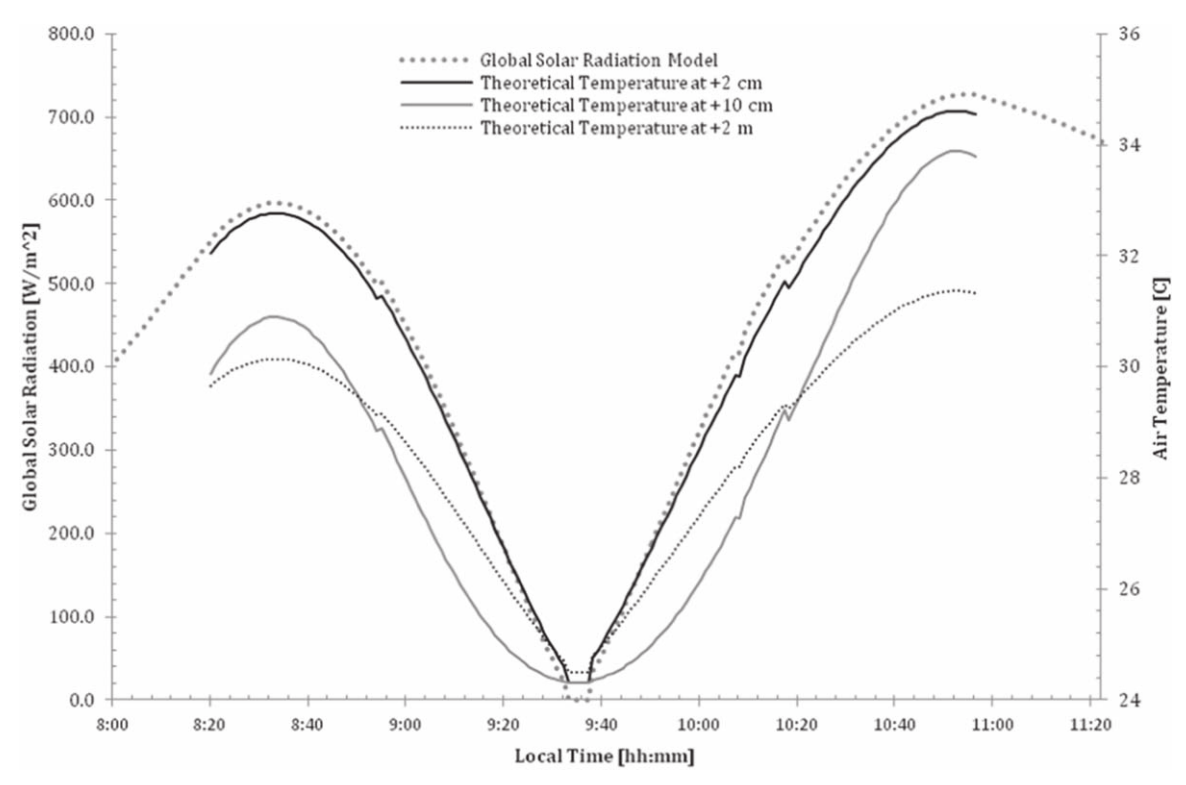


Figure 7. Theoretical curves illustrating our radiative model for global solar radiation (gray dots) (W m⁻²) and instantaneous air temperature (°C), at the indicated heights, as a result of the TSE on 2009 July 22, in Tianhuangping (Mt. Anji, Zheijang, China). Because they are all in phase, the models for this instantaneous temperature are used, instead of the global solar radiation variation due to the eclipse to study the NSAT lag and the delay function (the kinks of the curves observed at 8:50, 10:10 and 10:20 are artificial and come out from calculations of the occultation function).

Figures 11(a) and (b) depict the fluctuation results for 2 cm above the ground. In Figure 11(a), the regression curves are shown, and Figure 11(b) presents the temperature residual variation. Figure 11(c) gives the histogram of these residuals over the whole series of measurements along with its normal distribution. Table 3 displays variance values for the previously defined time sub-intervals. After 25 minutes from first contact the inhibition of convection begins to appear falling by approximately one order of magnitude in terms of variance (sub-interval B_I). In sub-interval C_I, around totality, the variance reaches a minimum (0.004 °C2). At 10:03 the convection begins to increase and, at 10:57 (fourth contact), it is already in a normal level. Note the similar variance values between the extremes sub-interval A_I and E_I. The analysis of NSAT fluctuation of residuals indicates that they exhibit almost a normal distribution as exemplified in Figure 11(b) or in Figure 11(c), with maximum oscillations of $\sim \pm 0.400$ °C in periods of higher convective activity and minimum of $\sim \pm 0.100$ °C near totality. The regression line fitted to all residuals, which is almost exactly equal to zero (Figure 11(b)), demonstrates a measure of smoothing quality made at the five different segments or sub-intervals in which the fluctuations were divided.

5.2. Case II (+10 cm)

On closer inspection, Figure 4 (or Figure 9) also reveals appreciable temperature fluctuations during most of the event at +10 cm. Specifically at the eclipse onset, we have sub-interval A_{II} from 08:21 to 08:50 followed by sub-interval B_{II} from 08:51 to 09:11. In the middle, we have sub-interval C_{II} with minimum fluctuations from 09:12 to 10:03. The fluctuations begin to increase again in sub-interval D_{II} from 10:04 to 10:30, and finally they amount to higher values in sub-interval E_{II} from 10:31 to 10:57. The results are shown in Figures 12(a)-(b) and in Table 4. The regression curves are portrayed in Figure 12(a) and Figure 12(b) provides graphically the corresponding residuals. From Table 4 we observe that 29 minutes past the first contact, the variance is reduced by a factor of 4.3, but in the next interval C_{II}, around totality, there is a reduction in the fluctuations by one order of magnitude. In the subsequent two sub-intervals D_{II} and E_{II}, the convective activity returns to similar levels as in the first two sub-intervals, respectively.

In comparing sub-interval $C_{\rm I}$ (Table 3) with sub-interval $C_{\rm II}$ (Table 4), we see that there has been a decline of variance by a factor of 0.5 around and during totality. We see a simultaneous diminishing of convection with height. Graphically, this effect

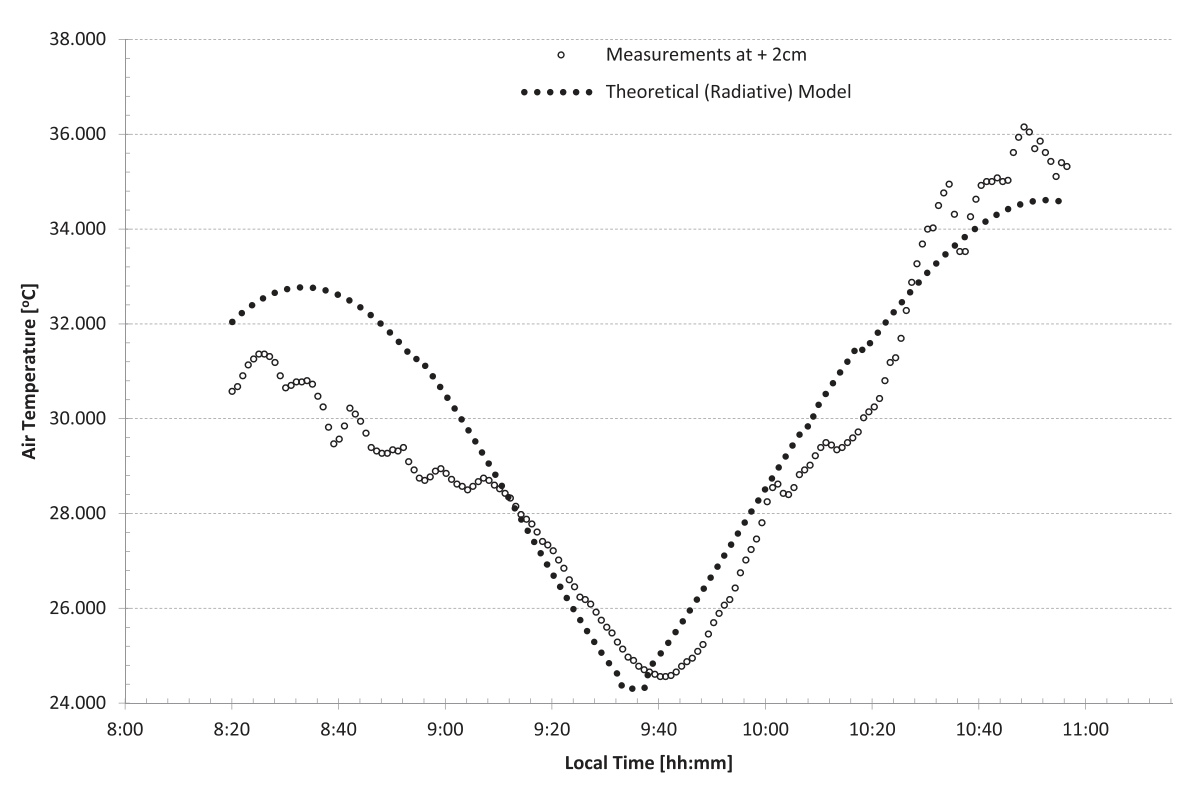


Figure 8. Theoretical radiative model (black dots) of NSAT at 2 cm above the ground. This theoretical curve is considered to be the virtually instantaneous response of the air to the TSE of 2009 July 22, at that height in Tianhuangping, because it is in phase with the solar radiation model described in Figures 5 and 7. Note that before totality approximately between 09:04 and 09:12 measured temperature coincides with T_{inst} , having no lag in that interval. In the previous interval there is a clear and significative unexpected negative lag until 09:12. After totality there are a least three times where both temperatures are equal, at 10:02, 10:28 and 10:36, approximately. Yet from the second of these times onwards there is an unexpected reversal of the lag with a small fluctuation where this third time is.

can be noticed examining Figure 12(b) in which the minimum fluctuations vary within the range of $\sim \pm 0.050\,^{\circ}\text{C}$. Extreme fluctuations of $\sim +0.400\,^{\circ}\text{C}$ and $-0.600\,^{\circ}\text{C}$, and of $\sim \pm 0.400\,^{\circ}\text{C}$ are observed in sub-intervals A_{II} and D_{II} , respectively; its corresponding variances in relation to sub-intervals A_{I} and D_{I} of Table 3 are quite similar in magnitude. This latter comparison means that no change in convectional activity was detected with a small change of height. Figure 12(b) also includes the regression line fitted to residuals, which, as before, is almost exactly equal to zero, demonstrating the quality of the smoothing (the histogram and its normal curve of Figure 12(c), show evidence of a normal distribution of NSAT residuals).

5.3. Case III (+2 m)

With regard to the third case, Figure 4 (or Figure 10) allows a general picture of the temperature fluctuations at 2 m above the ground. The distribution of these fluctuations with time appears quite different in relation to case II and I. For example, they are appreciable for a longer time (48 minutes), from first contact (08:21), than the other cases (29 minutes and 25 minutes, respectively). This time corresponds to sub-interval $A_{\rm III}$ from 08:21 to 09:09. Next, fluctuations drop off substantially from 09:10 to 09:43 (sub-interval $B_{\rm III}$) approaching totality as expected.

Yet, unlike case II and I, fluctuations unexpectedly begin to appear just after the minimum temperature from 09:44 to 10:15 (sub-interval $C_{\rm III}$). Perhaps other factors or mechanisms, different from convection, were at work, which may explain these specific fluctuations. Afterwards, fluctuations drop off again but in a lesser degree from 10:16 to 10:39 (sub-interval $D_{\rm III}$), and finally, from 10:40 to 10:57 (sub-interval $E_{\rm III}$), convective activity recovers its expected level. In terms of variance (see Table 5), one can realize that the minimum activity, noticed here in sub-interval $B_{\rm III}$, falls even more when compares to case II (sub-interval $C_{\rm II}$) and case I (sub-intervals $B_{\rm I}$ and $C_{\rm I}$). This result suggests that the convection suppression due to the eclipse increases with height during the event. Variance in extreme sub-intervals $A_{\rm III}$ and $E_{\rm III}$ display unsurprisingly maximum activity. Continuous sub-intervals $C_{\rm III}$ and $D_{\rm III}$ have similar intermediate values.

A graphic representation of fluctuation variation with time is given in Figure 13(b) where the reduction of fluctuations in the middle of the graph is quite clear. The dashed horizontal line in it, which is a regression linear fit, proves the smoothness and quality with which the procedure analysis has been made; Figure 13(c) provides the resultant histogram, showing an almost normal distribution of fluctuations. Its normal curve is also shown.

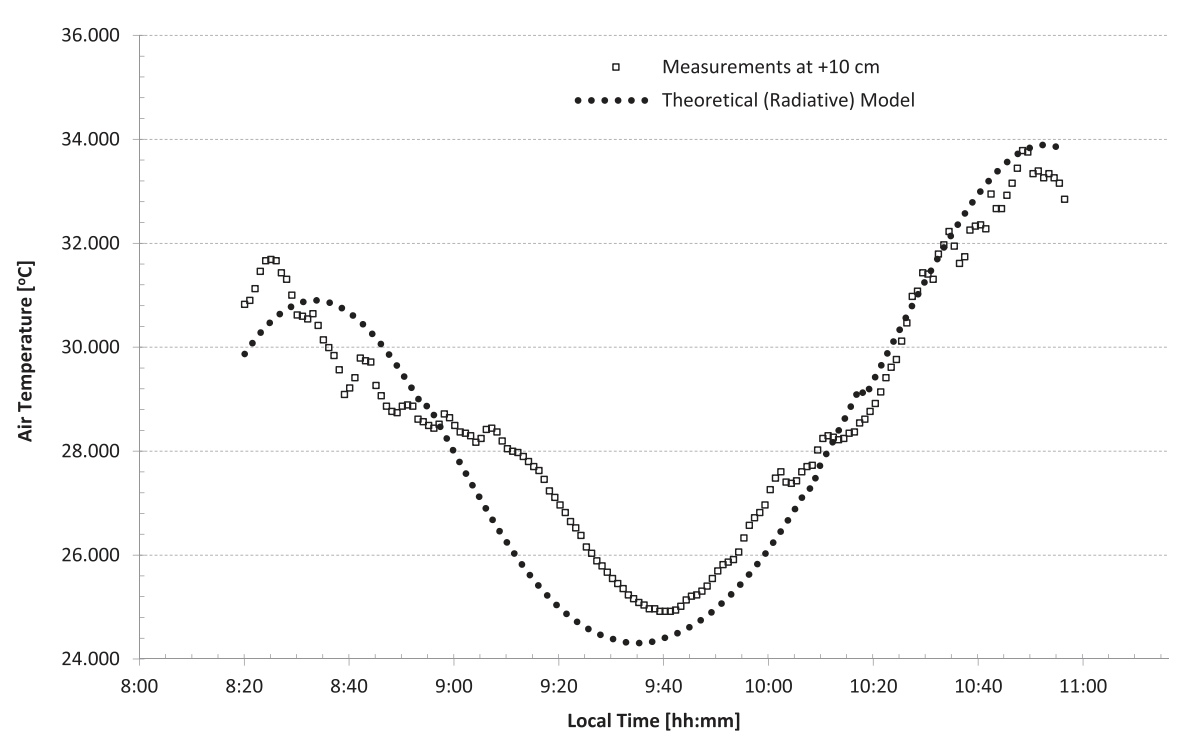


Figure 9. Theoretical radiative model (black dots) of NSAT at 10 cm above the ground. Similarly, it is considered as the virtually instantaneous response of the air to the TSE of 2009 July 22, at that height in Tianhuangping, because it is in phase with the solar radiation model described in Figures 5 and 7. Note that before totality there are at least two times where measured temperature is equal to $T_{\rm inst}$, approximately at 08:30 and 08:57; in between, there is an unexpected negative lag. After totality, at 10:13 measured temperature is equal to $T_{\rm inst}$. From this time up to 10:25 there is an unexpected reversal of the lag. From this time up to 10:45, approximately, values of measured temperature and $T_{\rm inst}$ are practically the same; after that this lag reversal continues until the end of the eclipse.

6. Discussion

In China other NSAT measurements were made within the TSE shadow track by different teams (Zainuddin et al. 2013; Stoeva et al. 2009; Pintér et al. 2010; Lu et al. 2011; Wu et al. 2011). To some extent a direct or strict comparison of the NSAT changes observed by these teams were not possible given the different ways how they found these changes or due to insufficient information available.

Lu's team observed the eclipse from a site located in Chongqing along the Changjiang river; they measured solar radiation, air temperature and RH at 1.5 m height at Chongqing University, 245 m above sea level (Huxi campus). In particular, they found that at 8:07, while the eclipse was still in progress, the temperature was still increasing, reaching a maximum of 31.2 °C at 8:17 before gradually decreasing and reaching a minimum of 28.8 °C at 9:16; this value was sustained until 9:25 when the temperature began to gradually increase again. Therefore, the NSAT decrease (in this case $\Delta T_{\rm absolute}$) was 2.4 °C during the eclipse. In order to determine the maximum drop in temperature caused by an eclipse, these authors chose two consecutive days with clear weather for comparison. From their Figure 3, it can be inferred that between July 21 and July 22, the variation and value of air temperature were similar outside the eclipse's time interval, and the difference in air temperature across two days was maximized at 9:24, with a maximum difference of 4.6 °C; therefore, this result gives an idea of how $\Delta T_{\rm linear}$ was for this eclipse in that location.

In the case of Pintér et al. (2010), whose team observed the eclipse in a site 130 km southwest from Shanghai, their results are presented in their Table 2 according to which they made measurements at four heights, namely, 10 cm, 50 cm, 1.5 m and 2.0 m. A drop of 8.0161 °C, 6.0852 °C, 4.9582 °C and 4.4022 °C were observed, respectively, taken from 1st contact to the instant of minimum temperature, which not correspond nor a linear anomaly neither an absolute anomaly as they are defined by Clark (2016). Instead, they correspond to ΔT as it is defined here in Table 2. Only two of these results are comparable as they correspond to the same height, say, that at 10 cm and 2.0 m; however, the degree to which land or surface type influences the immediate meteorological response to the reduction in solar radiation matters. The ability to compare these results with one another or with other measurements is severely limited because of the possible uncontrolled influences of the surface microclimate on the measurements in each case. This team reported windy conditions, that did not apply to our case, and some clouds during the eclipse. Our instruments were installed in a greenvegetation environment at 809 m above sea level. The vegetative and soil moisture differences of different sites may alter

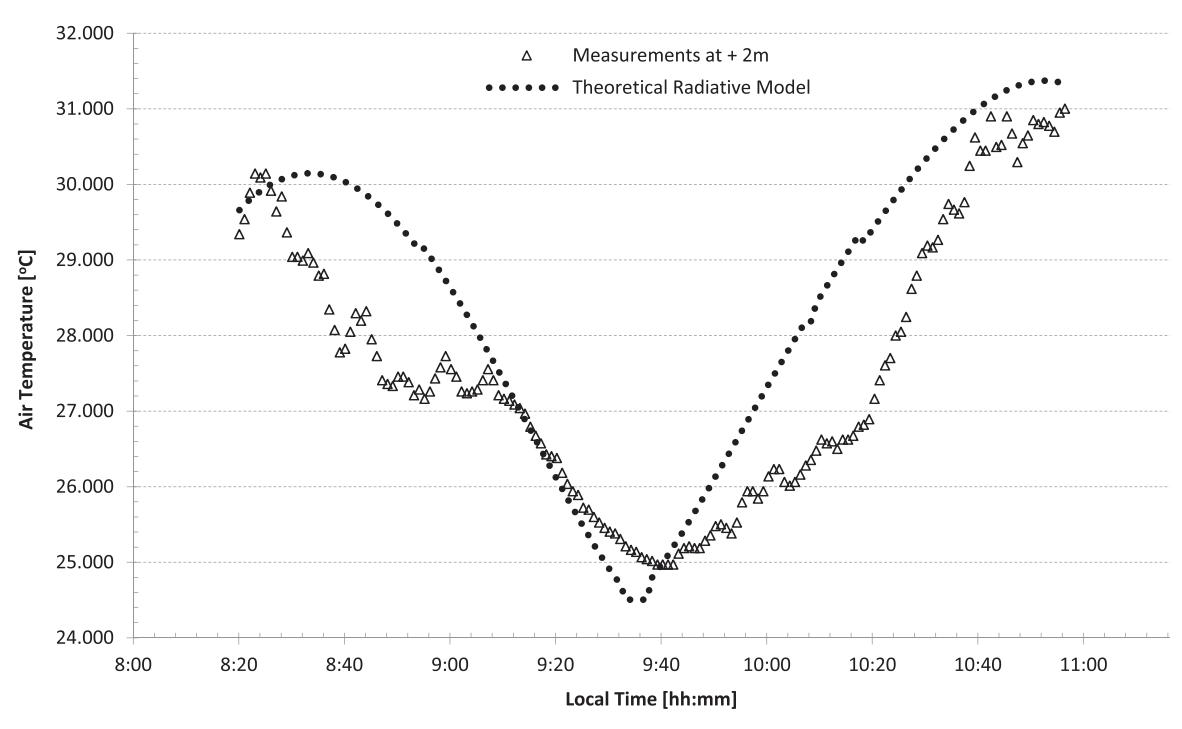


Figure 10. Theoretical radiative model (black dots) of NSAT at 2 m above the ground. Equally, it is considered as the virtually instantaneous response of the air to the TSE of 2009 July 22, at that height in Tianhuangping, because it is in phase with the solar radiation model described in Figures 5 and 7. As in the previous cases, there is an unexpected negative lag before totality, between 08:26 and 09:12. Between 09:12 and 09:19 values of measured temperature are equal to T_{inst} . Afterward, the lag is as expected for the rest of the eclipse.

significantly the local response to a radiative reduction by action of a TSE. But, unfortunately, these researchers did not identify the particular micrometeorological environment in which the measurements were taken. The only information that we were able to get from their observation-site coordinates was that they were next to the sea. Thus, any possible comparison is approximate and not identical.

Stoeva's team (Stoeva et al. 2009), observed very close to our observation site at three different heights of 10 cm, 50 cm and 2 m; their results are reproduced in Figure 14 and Table 6 (numerical values of temperature drops are estimated by the difference between the minimum and maximum temperatures plotted in Figure 14). In comparison to Stoeva et al. (2009) our observed temperature trends are similar, with clouds producing similar effects in the early stages of the eclipse; however, we measure a smaller temperature drop at 10 cm. The difference may be explained by local micrometeorological and observing conditions. They used an instrument resolution of 0.1 °C and show images of the equipment setup and its environment. We note that the ground appeared to be a combination of pieces of concrete surrounded by dried greenish-grass. Although our sensors were located very close to where their sensors were, there was a marked differentiation in surface albedo, which could potentially explain some difference between their observations and our measurements.

Pintér et al. (2010), on the other hand, observing from a point close to Shanghai found the same effect as ours in their measurements at four different heights (see Table 6) before totality (see their Figures 2(b)–(e)), which may also be attributable to clouds at their observing site.

Searching for the effects of this TSE on photooxidants in different areas of China, Wu et al. (2011) made observations of NSAT within the umbra at a height of 2 m in Chongqing and Wuhan airports (416 m above sea level and 35 m above sea level, respectively). According to the information given by these authors, taken from a satellite image (see their Figure 1(a)), Wuhan was influenced by a light cloud cover but Chongqing was influenced to a lesser extent, and there was no rain during the solar eclipse period according to the local observations in both sites. These observations were modeled and were compared with a simulated run with no yielding, at the instant of minimum temperature, a (quasi-linear) anomaly of 2.12 °C for the first and 2.03 °C for the second (see their Figures 3(c) and (d)). In Table 6 we attempt to give a first comparison of all these results.

As can be observed from this table, based on a comparison between teams, there is a general decrease tendency of ΔT , $\Delta T_{\rm linear}$ and $\Delta T_{\rm absolute}$ with height for all places. Also, it seems apparently that there is an approximation between values of $\Delta T_{\rm linear}$ and $\Delta T_{\rm absolute}$ as long as height increases. The best

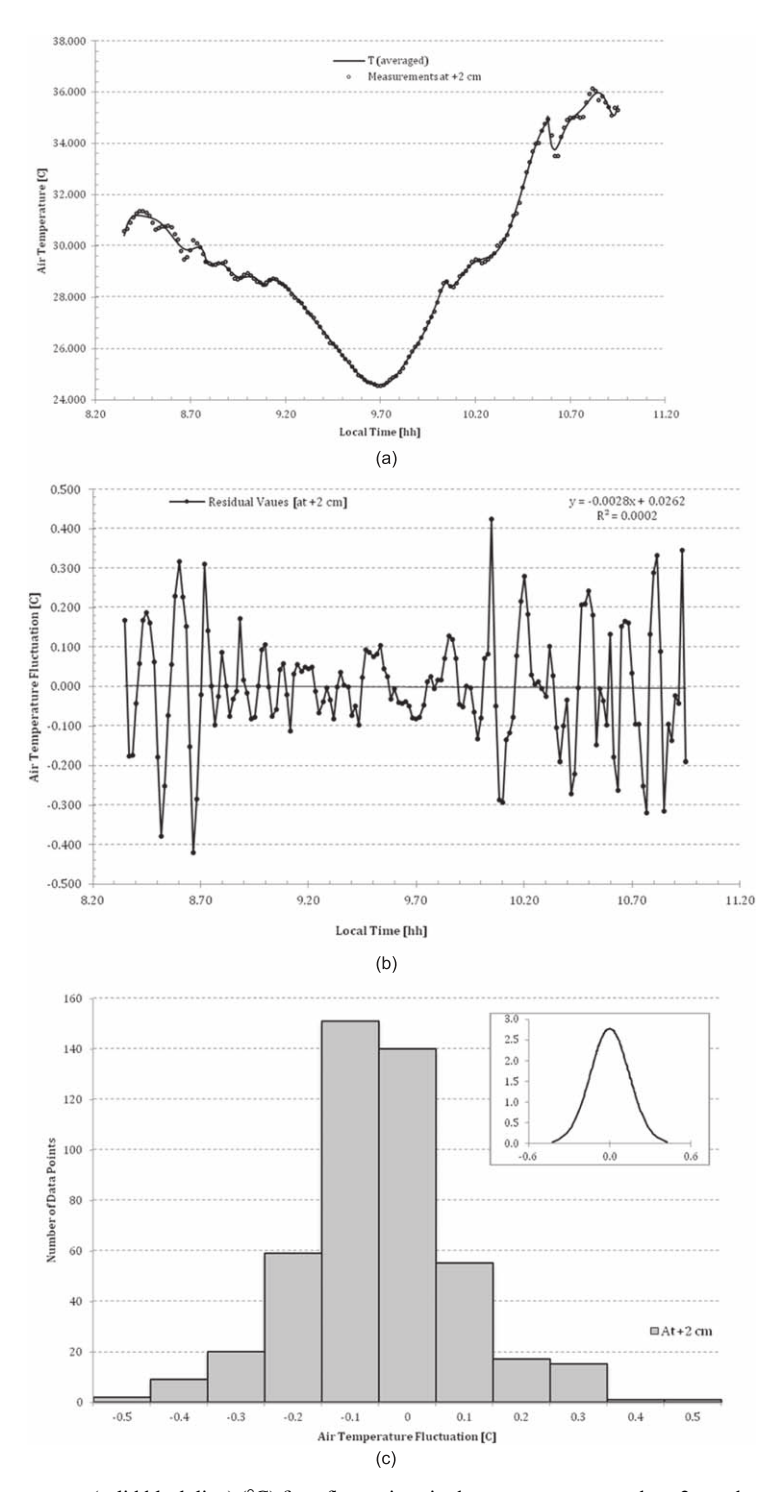


Figure 11. (a) The model of mean temperature (solid black line) ($^{\circ}$ C) fit to fluctuations in the measurements made at 2 cm above the ground. A polynomial regression fit has been applied sector-by-sector depending on the dispersion of measurements. (b) NSAT residuals around the mean temperature ($^{\circ}$ C) given by regression fit in Figure 11(a), at +2 cm. It is clearly seen a decreasing of temperature fluctuations between 8.80 hr (09:48) and 10.00 hr (10:00) due to the eclipse; outside of this interval, the fluctuations are greater. The regression line fitted to these residuals (almost zero) indicates the quality of the smoothing procedure. (c) The histogram of NSAT residuals ($^{\circ}$ C), over the whole series of measurements, presented in Figure 11(b) at 2 cm above the ground. A normal distribution curve fit is shown in the upper right corner inset.

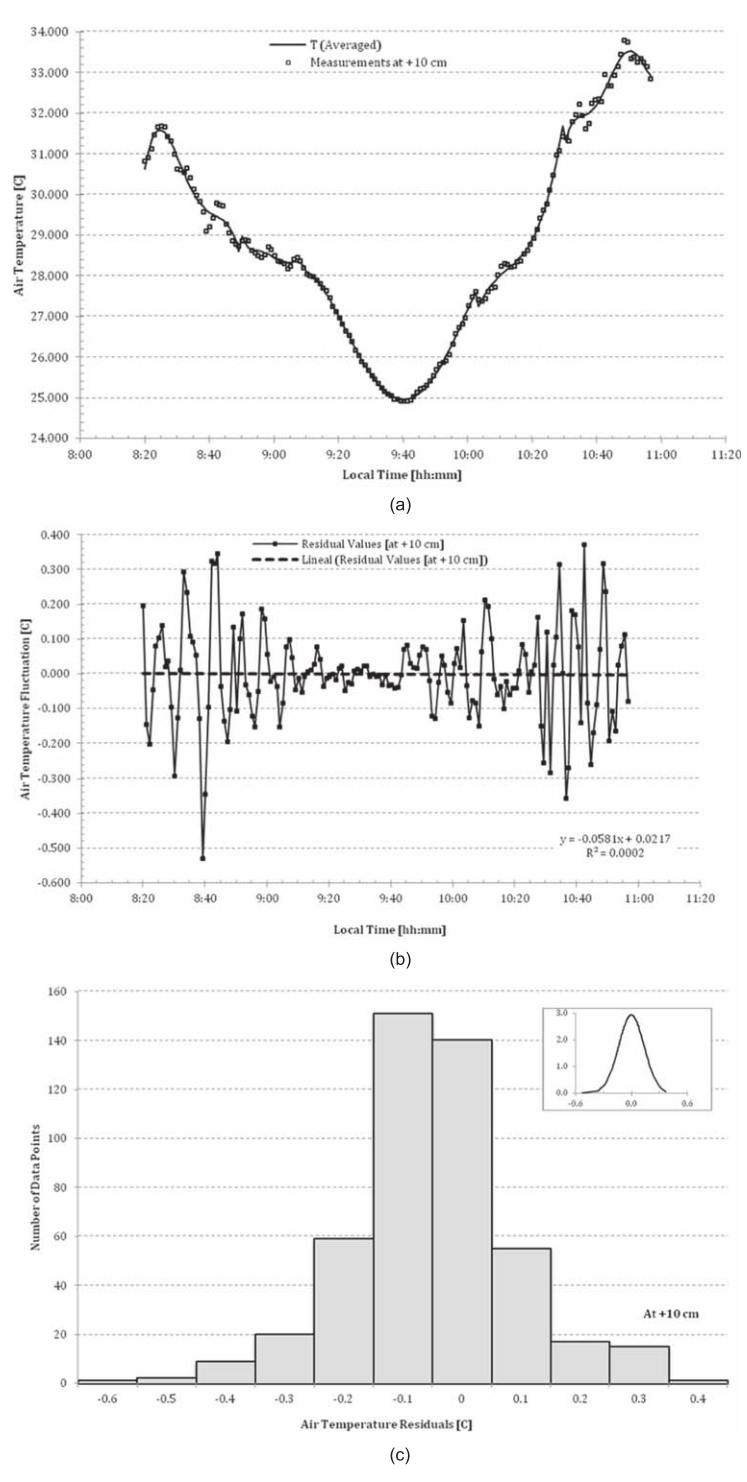


Figure 12. (a) The model of mean temperature (solid black line) ($^{\circ}$ C) fit to fluctuations in the measurements made at 10 cm above the ground. A polynomial regression fit has been applied sector-by-sector depending on the dispersion of measurements. (b) NSAT residuals ($^{\circ}$ C) around the mean temperature given by a regression fit in Figure 12(a), at +10 cm. A reduction of temperature fluctuations even greater than at +2 cm, between 09:10 and 09:45 due to the eclipse is noted; out of this interval, the fluctuations are greater. The regression (dashed) line fitted to these residuals (almost zero) indicates the quality of the smoothing procedure made through the entire period of time. (c) The histogram of air temperature residuals ($^{\circ}$ C), over the whole series of measurements, presented in Figure 12(b) at 10 cm above the ground. A normal distribution curve fit is shown in the upper right corner inset. It is skewed a little to the left.

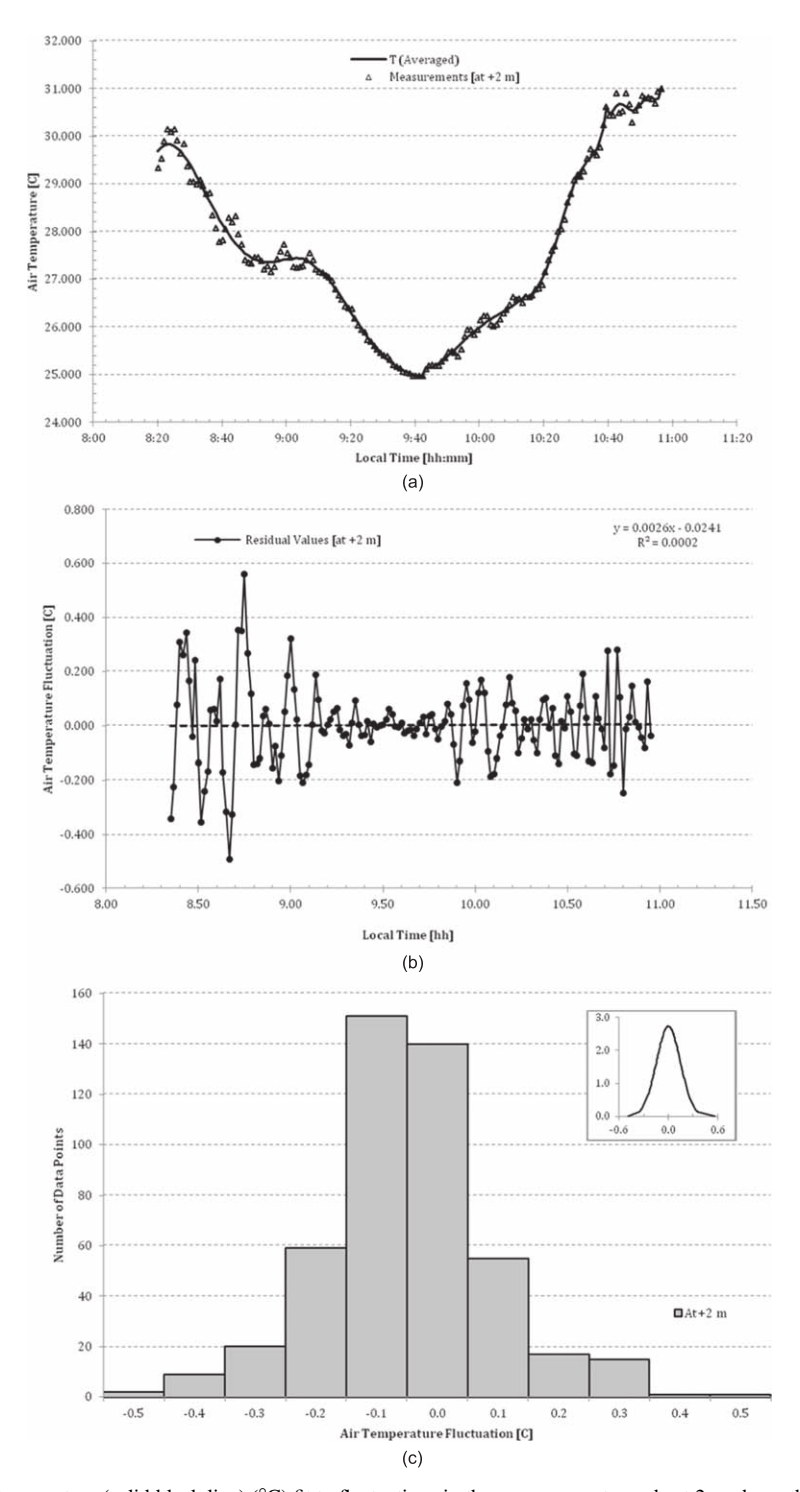


Figure 13. (a) The model of mean temperature (solid black line) ($^{\circ}$ C) fit to fluctuations in the measurements made at 2 m above the ground. A polynomial regression fit has been applied sector-by-sector depending on the dispersion of measurements. (b) NSAT residuals ($^{\circ}$ C) around the mean temperature given by regression fit in Figure 12(a), at 2 m. The reduction of temperature fluctuations observed between 9.2 hr (09:12) and 9.8 hr (09:48) due to the eclipse, is even greater than at +10 cm; out of this interval, the fluctuations are greater. The regression (dashed) line fitted to these residuals (almost zero) indicates the quality of the smoothing procedure. (c) The histogram of air temperature residuals ($^{\circ}$ C), over the whole series of measurements, presented in Figure 12(b) for 2 m above the ground. A normal distribution-curve fit is shown in the upper right corner inset. Also, it is skewed a little to the right.

Publications of the Astronomical Society of the Pacific, 132:114503 (20pp), 2020 November Peñaloza-Murillo, Roman, & Pasachoff

Table 3

Time Sub-intervals for Analysis of the NSAT Fluctuations, at +2 cm, Due to Convection During the TSE of 2009 July 22, at Tianhuangping (Zhejiang), China

Time Sub-intervals						
$oxed{A_{I}} oxed{B_{I}} oxed{C_{I}} oxed{D_{I}}$						
Interval	08:21-08:46	08:47-09:06	09:07-10:02	10:03-10:35	10:36-10:57	
Duration (minutes)	25	19	55	32	21	
Coefficient of determination (R^2)	0.8709	0.9497	0.9979	0.0031	0.9193	
Variance (°C ²)	0.043	0.005	0.004	0.030	0.042	

Note. The table includes the results for the coefficients of determination values and variance per sub-interval.

Time Sub-intervals						
$egin{array}{cccccccccccccccccccccccccccccccccccc$						
Interval	08:21-08:50	08:51-09:11	09:12-10:03	10:04-10:30	10:31–10:57	
Duration (minutes)	29	20	51	26	26	
Coefficient of determination (R^2)	0.9519	0.8032	0.9979	0.9909	0.9269	
Variance (°C ²)	0.043	0.010	0.002	0.012	0.038	

Note. The table includes the results for the coefficients of determination values and variance per sub-interval.

Table 5
Time Sub-intervals for Analysis of the NSAT Fluctuations, at +2 m, due to Convection During the TSE of 2009 July 22, at Tianhuangping (Zhejiang), China

Time Sub-intervals					
	$A_{\rm III}$	$B_{\rm III}$	$C_{\rm III}$	$\mathrm{D_{III}}$	E _{III}
Interval	08:21-09:09	09:10-09:43	09:44-10:15	10:16-10:39	10:40-10:57
Duration (minutes)	48	33	31	23	17
Coefficient of determination (R^2)	0.9519	0.8032	0.9979	0.9909	0.9269
Variance (°C ²)	0.050	0.001	0.010	0.009	0.020

Note. The table includes the results for the coefficients of determination values and variance per sub-interval.

comparison to be made with our results is that of Stoeva et al.'s results given that both teams were practically at the same observation site, but according with their statement it is quite surprising the significant outcome that they found of no variation at all of NSAT with height, which is a very unexpected response and opposite what we observe on their graphs (Figure 14).

The team of Zainuddin et al. (2013) observed the eclipse under cloudy conditions at Wild Resort area in Hangzhou (Zhejiang). Their NSAT are shown in their graph 2 where a value of 29.9 °C is given as maximum temperature at 2nd contact, and a value of 27.9 °C is given as minimum temperature but before 3rd contact. Thus, a decrease of 2.0 °C occurred in this interval, which does not correspond to any anomaly considered in this work. Also, these authors do not give at what height above the ground these measurements were taken; hence, this additional anomaly was not included in Table 6.

The activity of the atmospheric boundary layer, extensively studied in the past during this type of phenomenon, were investigated this time, for the 2009 TSE in China, by He et al. (2010) and Chen et al. (2011) from ceilometer observations and meteorological measurements, respectively, over Heifei, not very far away from Shanghai. Yet in our case this activity was studied at Tianhuangping by simply analyzing the fluctuations of air temperature following the same methodology as that we used in our previous paper (Peñaloza-Murillo & Pasachoff 2015), based on an earlier paper by Szałowski (2002).

In consideration of Tables 3–5, giving the variance as indicator of the activity of the atmospheric boundary layer, for different time intervals at different heights, we have the following comparison shown in Table 6. Reading this table horizontally (that is, versus time) one can see that minimum fluctuations tend to occur at intermediate sub-intervals with emphasis in sub-intervals B and C for all heights; reading it vertically (that is, versus height) the fluctuations are seldom

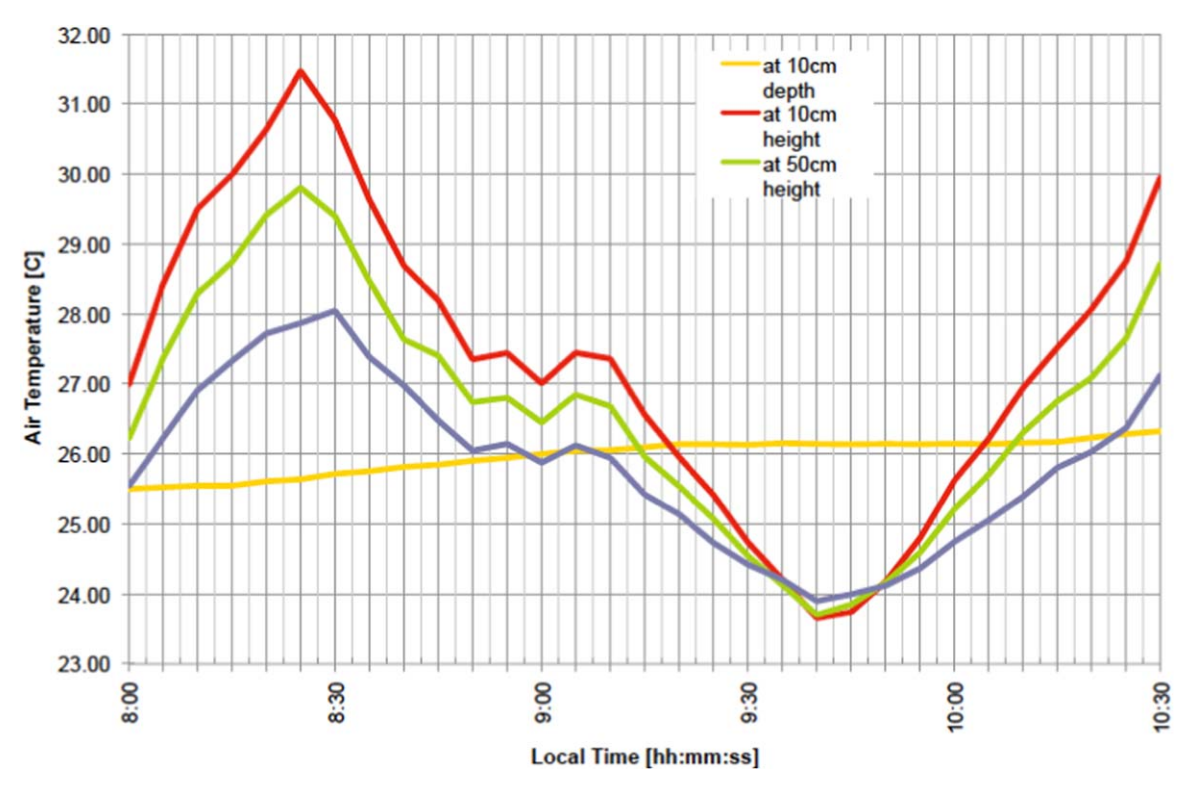


Figure 14. NSAT measurements (in °C) made by Stoeva et al. (2009) at Tianhuangping during the 2009 TSE, between 08:00 am and 10:30 am (LT). The blue line corresponds to a height of 200 cm above the ground. (Reprinted with permission from Stoeva et al. 2009.)
(A color version of this figure is available in the online journal.)

Table 6

Different Air Temperature Negative Anomalies Near the Surface Produced by the Longest Total Solar Eclipse of the 21st Century in 2009 July 22, at Different Sites of China

				ΔT
Height (cm)	$\Delta T(^{\circ}C)$	ΔT_{linear} (°C)	$\Delta T_{\rm absolute}$ (°C)	(°C) (?)
2	6.01	8.42	6.80	
10	5.90 8.02 ^P	7.07	6.77	7.8 ^S
50	6.01 ^P			6.1 ^S
150	4.96 ^P	4.6 ^L	2.4 ^L	
200	4.37 4.40 ^P	5.27 (2.12 ^{Ch} , 2.03 ^{Wuh}) ^W	5.17	4.1 ^S

Note. Bold figures are values of this work. (P) Values from Pintér et al. (2010) estimated from measurements taken 130 km south from Shanghai at approximately 0 m above sea level (asl). (S) Values of Stoeva et al. (2009) graphically estimated in this work from measurements taken very close to our observation site (809 m asl) by that team. (W) Values from Wu et al. (2011) taken at Chongqing airport (Ch) (416 m asl) and Wuham airport (Wuh) (35 m asl). (L) Values from Lu et al. (2011) taken at Huxi campus, Chongqing University (245 m asl).

variable. This result is a clear indication that convective turbulence tends to diminish during the fall in temperature, a typical result analogous to that during daily sunsets. Possibly cloudiness deepens even more the convective turbulence decrease in comparison to a cloudless sky (see Gorchakov et al. 2008; Peñaloza-Murillo & Pasachoff 2015). In relation to this, these authors, working with the afternoon TSE of 2006 March 29, over Kislovodsk (Russia) and on 2001 June 21, over Lusaka (Zambia, Africa) made analysis of its convective activity calculating the air temperature variance. In those cases, they found higher results than ours indicating less stability. From these last eclipses it can be seen that the tendency toward a steadily and irreversible decreasing convective activity is remarkable for an afternoon TOS in relation to a morning eclipse where there is a reversal of it afterwards (see Figures 8–10 or Figures 12–13 and Figure 8 of Szałowski 2002). However, in comparing our results (Table 7) with those from the latter author it can also be seen that it was found a higher convective activity for the morning 1999 solar eclipse, which was observed at Szczawnica, Poland (see Table 3 of Szałowski 2002), than that of the morning 2009 TSE at Tinhuangping, a clear indication of the cloudiness effect over convection.

Table 7

Air Temperature Variance at Different Heights During the TSE on 2009 July 22, at Tianhuangping, China

Height	Variance (°C ²)					
	Sub-intervals A _{I,II,III}	Sub-intervals B _{I,II,III}	Sub-intervals $C_{I,II,III}$	Sub-intervals D _{I,II,III}	Sub-intervals E _{I,II,III}	
+2 cm (I)	0.043	0.005	0.004	0.030	0.042	
+10 cm (II)	0.043	0.010	0.002	0.012	0.038	
+2 m (III)	0.050	0.001	0.010	0.009	0.020	

Note. The time sub-intervals are not equal but have approximately the same length (see Tables 3-5). Near totality the atmospheric layer near the surface seems to become rather stable.

The discussion of the calibration curves involves a matter over a novel method already developed in our previous paper (Peñaloza-Murillo & Pasachoff 2015), which was based on an early methodology suggested by Phillips (1969). Bearing in mind the cloudiness, it was a complicated task to derive these curves in comparison with the case where the sky was clear, i.e., in Zambia in 2001 (Peñaloza-Murillo & Pasachoff 2015). Curves like these have never been published before; however, we think that they are consistent and reliable given their performance in reproducing the instantaneous temperature profiles which will be used in our subsequently analysis of NSAT lag in relation to solar radiation (see Figure 7).

7. Conclusions and Final Comments

Though totality was visible (Petrov et al. 2010; Pasachoff et al. 2011), variable cloudiness complicated observations and our subsequent interpretation of the thermal response of the atmosphere due to the eclipse. Despite the cloudy conditions (Peñaloza-Murillo & Pasachoff 2018), the method applied in this investigation turns out to be practical and it is affordable to be repeated and rechecked in future similar conditions. In other words, using a simple set of NSAT measurements obtained during solar eclipses even under adverse weather allows a mathematical analysis of these measurements and its relation to changes and fluctuations of it can still be attempted following the methods presented here (Phillips 1969; Szałowski 2002) along with that presented by Peñaloza-Murillo & Pasachoff (2018) in which an analysis of the cloudiness and solar radiation during this eclipse was undertaken.

The anomalous discrepancies displayed in Table 6 are indications of the different ambient conditions in which the respective measurements of NSAT were obtained by different teams in China although some trends were, in principle, detected during this eclipse. Our team confirmed the detection of cloudiness effects over NSAT measurements during the eclipse in terms of the lag reversals found before and after totality in accordance with other works (Huzimura 1949; Winkler et al. 2001; Aplin & Harrison 2003). Moreover, the observations made by another two teams, one of them observing far away from our site, seem to reveal also the same effects.

It seems that the technic of applying a virtual variable, defined and used here and in our previous work (Peñaloza-Murillo & Pasachoff 2015) as "instantaneous temperature," implicitly suggested by Phillips (1969) via "calibration curves," is a workable and convenient way of studying the temperature response during a TSE.

The measurements confirm that the occurrence of a stable stratification in the low boundary layer can be expected due to a total solar eclipse. The general fall of convection intensity is visible in temperature fluctuation component variance decrease. The temporal scales of convection analyzed on the basis of temperature fluctuating component variance, obtained inside 157.2 minutes (2.62 hr) maximum eclipse-centered time range, seems to be different from ones observed under typical or normal conditions of cloudless skies (Peñaloza-Murillo & Pasachoff 2015). Therefore, it is important to separate the effects of the eclipse from those of the changeable cloud cover, but the increase of the temporal scale seems to take place. The separation of cloudiness effects as well as the issue related to negative lags attributable to cloudiness that we found in this investigation will be a focus of our forthcoming third and final study on the thermal response of the air temperature near the surface, produced by the longest total solar eclipse of the 21st century at Tianhuangping (Zhejiang), China on 2009 July 22, under cloudy skies.

The participation of the first co-author, M.P.-M., in the Williams College Expedition to China was possible by a generous partial grant from the Association of Professors of the University of the Andes, APULA (Mérida, Venezuela). The mathematical analysis of the temperature measurements, made during this expedition, were carried out by M.P.-M. as a Fulbright visiting scholar on sabbatical leave (2012), supported by a Fulbright fellowship (Grantee ID: 68110145), at the Hopkins Observatory of Williams College (Williamstown, MA), which he thanks for its hospitality; the help provided by the University of the Andes (ULA) and the international Fulbright program for exchange of scholars, is acknowledged. M.P.-M. also thanks Denise Buell, the Dean of the Faculty of Williams College, for supporting his 2018–2019 visits. Co-author M.T.R. wishes to acknowledge the support of his fellow co-author, J.M.

P., for graciously welcoming and hosting him as part of the Williams College expedition to China. M.T.R. also wishes to acknowledge the support of his then graduate advisor at Cornell University, Prof. Peter Gierasch, who happily permitted MTR to take leave with the intent to make measurements and witness the unique beauty of a total solar eclipse. We are grateful to Yihua Yan of the National Solar Observatory, Beijing, and Jin Zhu, Beijing Planetarium, for their assistance with site selection in a reconnoitering trip in 2008. We thank Mark Sood of A Classic Tours Collection for travel assistance. We express our gratitude to Chenyang Sun, Williams College Class of 2022, for his help in the Chinese translation of one of the papers used in this investigation while M.P.-M. was visiting the Astronomy Department of Williams College in 2019. The Williams College Expedition to China was sponsored in large part by grant 8436-08 from the Committee for Research and Exploration of the National Geographic Society. J.M.P. thanks John Mulchaey for his sabbatical hospitality at the Carnegie Observatories during the completion of this paper. Mika Hirai of Williams College's Office of Information Technology was very generous in providing the final sketch of Figure 2. Current eclipse research at Williams College receives major support from grant AGS-1903500 from the Solar Terrestrial Program, Atmospheric and Geospace Sciences Division, U.S. National Science Foundation. Finally, material support for correcting the proof of this paper was provided by the Graduate Studies Council of the University of the Andes, Venezuela, which is appreciated with gratitude by M. P.-M.

ORCID iDs

Marcos A. Peñaloza-Murillo, https://orcid.org/0000-003-4046-1031

Michael T. Roman https://orcid.org/0000-0003-3490-0456 Jay M. Pasachoff, https://orcid.org/0000-0002-4372-4928

References

```
Alexander, S. 1854, AJ, IV, 17
Aplin, K. L., & Harrison, R. G. 2003, RSPSA, 459, 353
Brerenton, J. A. 1834, The Boston Medical and Surgical Journal 10, 296
Chen, Z., Liu, W., Zhang, Y., He, J., & Ruan, J. 2011, OptLT, 43, 50
Chung, Y., Kim, H., & Choo, S. 2010, Air Quality, Atmosphere & Health, 3, 125
Clark, M. R. 2016, RSPTA, 374, 2077
Clayton, H. 1901, AnHr, 43, 5
Espenak, F. 2014, Thousand Year Canon of Solar Eclipses 1501 to 2500
(Portal, AZ: AstroPixels Publishing), 294
```

```
Espenak, F., & Anderson, J. 2008, Total Solar Eclipse of 2009 July 22. NASA/
   TP-2008-214169
Gorchakov, G. I., Kadygrov, E. N., Kortunova, Z. V., et al. 2008, IzAOP,
  44, 100
Gray, S., & Harrison, R. 2012, RSPSA, 468, 1839
Hanna, E. 2000, Wthr, 55, 430
He, J., Liu, W., Zhang, Y., et al. 2010, ChOpL, 8, 439
Huzimura, I. 1949, in Report of Solar eclipse Observation May, 9 1948. The
   23 Geophysical Magazine (Central Meteorological Observatory: Tokyo),
Jeon, B-II. 2011, Journal of Environmental Science International, 20, 1041
Jeon, B-II., & Oh, I-B. 2011, Journal of Environmental Science International,
  20. 1049
Kadygrov, E. N., Miller, E. A., & Troitsky, A. V. 2013, ITGRS, 51, 4672
Krause, J. K., & Dodrill, B. C. 1986, RScI, 57, 661
Kumar, A. 2014, InJPh, 88, 449
Kwak, K., Ryu, Y., & Baik, J. 2011, JApMC, 50, 500
Leeds-Harrison, P., Young, E., & Blackburn, D. 2000, Eur. J. Soil Sci., 51, 183
Lu, J., Chen, S. L., Bu, C. W., & Liu, Y. 2011, Spectroscopy and Spectral
  Analysis, 31, 911, (in Chinese with abstract in English)
Meeus, J. 2002, More Mathematical Astronomy Morsels (Richmond, VA:
   Willmann-Bell)
Morecroft, M., Oliver, H., Stokes, V., & Morison, J. 2000, Wthr, 55,
Nieuwstadt, F., & Brost, R. 1986, JAtS, 43, 532
Pasachoff, J. M. 2009, RAA, 9, 613
Pasachoff, J. M. 2017, NatAs, 1, 0190
Pasachoff, J. M., Rusin, V., Saniga, M., Druckmüllerová, H., & Babcock, B. A.
   2011, ApJ, 742, 29
Peñaloza-Murillo, M. A., & Pasachoff, J. M. 2015, JASTP, 125, 59
Peñaloza-Murillo, M. A., & Pasachoff, J. M. 2018, JGRD, 123, 13443
Petrov, N., Duchlev, P., & Koleva, K. 2010, BlgAJ, 14, 102
Phillips, K. 1969, JBAA, 79, 460
Pintér, T., Péntek, K., & Mitre, Z. 2008, in 19, Celoštátny Sinečný Seminár,
  Papradno 2008: Zbornia Referátov ed. M. Lacković & P. Ambrož Kasico
  a.s. 2008 (Bratislava: Slovakia), 106
Pintér, T., Péntek, K., & Mitre, Z. 2010, in 20th National Solar Physics
  Meeting Conference Proceedings, ed. I. Dorotovic Slovack Central
  Observatory (Hurbanovo: Slovakia), 144
Rabin, R., & Doviak, R. 1989, JApMe, 28, 1226
Rao, K., Reddy, N., Ramakrishna, G., et al. 2013, JASTP, 95, 87
Segal, M., Turner, R. W., Prusa, J., Bitzer, R. J., & Finley, S. V. 1996, BAMS,
Stoeva, P., Stoev, A., Kuzin, S., Stoyanov, N., & Pertsov, A. 2009, in Fundamental Space Research 2009, ed. T. Dachev, D. Danov, &
   Y. Tishchenko Solar Terrestrial Influences Institute "Acad. D. Mishev" of
  Bulgarian Academy of Science, Sofia, Bulgaria & Kotel'nikov Institute of
  Radioengineering and Electronics of Russian Academy of Sciences,
  Moscow, 132
Szałowski, K. 2002, J. Atmos. Sol. Terr. Phys., 64, 1589
Tzanis, C. 2005, Journal of Remote Sensing, 26, 3585
Wang, K.-Y., & Liu, Ch.-H. 2010, GeoRL, 37, L01804
Winkler, P., Kaminski, U., Köhler, U., et al. 2001, MetZe, 10, 193
Wu, J.-B., Wang, Z., Zhang, W., et al. 2011, ACP, 11, 8075
Zainuddin, M., Haron, S., Niri, M., et al. 2013, Middle-East Journal of
  Scientific Research, 13, 220
```